Positive Feedback Between Contractile Ring Myosin and Ring-Directed Cortical Flow Drives Cytokinesis

Renat N. Khaliullin[1]*, Rebecca A. Green[1], Linda Z. Shi[2], J. Sebastian Gomez-Cavazos[1], Michael W. Berns[2], Arshad Desai[1], and Karen Oegema[1]*

[1]Department of Cellular and Molecular Medicine, Ludwig Institute for Cancer Research, University of California, San Diego, La Jolla, CA 92093, USA.

[2]Department of Bioengineering and Institute of Engineering in Medicine, University of California, San Diego, 9500 Gilman Drive, La Jolla, CA, 92093, USA

*Correspondence to: Karen Oegema (koegema@ucsd.edu); Renat N. Khaliullin (renatkh@gmail.com)

ABSTRACT

During cytokinesis, an equatorial actomyosin contractile ring rapidly transforms cell shape by constricting at a relatively constant rate despite its progressively decreasing size. The closure rate per unit length of the ring must accelerate as the ring gets smaller to maintain the overall constant rate of closure. Here, we examine the mechanistic basis for this acceleration by generating a 4D map of cortical flow in conjunction with monitoring ring component dynamics during the first division of the *C. elegans* embryo. This analysis reveals that acceleration arises because ring myosin pulls on the adjacent cortex generating ring-directed cortical flow that, in turn, accelerates constriction by delivering cortical myosin into the ring. We derive an analytical mathematical formulation that captures the positive feedback-dependent evolution of the contractile ring and use this formulation to provide a non-intuitive explanation for why reducing myosin activation by rho kinase inhibition slows contractile ring closure.

IMPACT STATEMENT: During cytokinesis, positive feedback between myosin motors in the contractile ring and ring-directed cortical flow drives constriction rate acceleration to ensure timely cell separation.

MAJOR SUBJECT AREAS: Cell biology, Computational and Systems Biology

KEYWORDS: contractile ring, cortical flow, positive feedback, analytical mathematical model, rho kinase, LET-502, myosin II, anillin

INTRODUCTION

During cytokinesis in animal cells, constriction of an equatorial actomyosin ring cinches the mother cell surface to generate a dumbbell-shaped structure with an intercellular bridge that connects the two daughter cells (Fededa & Gerlich, 2012; Green, Paluch, & Oegema, 2012). The contractile ring assembles in response to the equatorial activation of RhoA (Green et al., 2012; Jordan & Canman, 2012; A. Piekny, Werner, & Glotzer, 2005), which patterns the cortex by recruiting contractile ring components from the cytoplasm (Vale, Spudich, & Griffis, 2009; Yumura, 2001; Zhou & Wang, 2008). Recent work in the *C. elegans* embryo suggests that the equatorial cortex is compressed after this initial patterning, leading to the alignment of actin filament bundles as the ring forms (Reymann, Staniscia, Erzberger, Salbreux, & Grill, 2016). After its assembly, the ring is thought to progressively disassemble as it constricts (Murrell, Oakes, Lenz, & Gardel, 2015; Schroeder, 1990). Ring constriction must complete within a short cell cycle window during mitotic exit (Canman, Hoffman, & Salmon, 2000; Martineau, Andreassen, & Margolis, 1995; Straight et al., 2003). Timely constriction relies on the conserved ability of contractile rings to maintain a relatively constant closure rate despite their progressively decreasing perimeter (Biron, Libros, Sagi, Mirelman, & Moses, 2004; Bourdages, Lacroix, Dorn, Descovich, & Maddox, 2014; Calvert et al., 2011; Carvalho, Desai, & Oegema, 2009; Ma et al., 2012; Mabuchi, 1994; Pelham & Chang, 2002; Zumdieck, Kruse, Bringmann, Hyman, & Julicher, 2007). This property implies that rings close at a faster rate per unit length as they get smaller. Prior work postulated that this acceleration arises because force generators, either myosin motors (Wu & Pollard, 2005) or actin filament-based contractile units (Carvalho et al., 2009), are retained during constriction, leading to an increase in their amount per unit length. This retention model presumes that acceleration arises from processes intrinsic to the contractile ring, ignoring potential influence of interactions between the ring and the adjacent cortex.

Here, we examine the role of interactions between the ring and surrounding cortex on contractile ring dynamics in the *C. elegans* embryo. Through 4D analysis of cortical flow in conjunction with monitoring of ring component dynamics during closure, we show that acceleration of the per unit length constriction rate does not arise from ring-intrinsic component retention, but instead results from positive feedback between ring myosin and ring-directed cortical flow. We derive an analytical mathematical formulation that captures the positive feedback-dependent evolution of the contractile ring and employ it to analyze experimental data to assess the effects of rho kinase inhibition, uncovering a new, non-intuitive explanation for why reducing myosin activation by rho kinase inhibition slows ring closure.

RESULTS

The cortex at the cell poles expands in response to tension generated by the constricting ring, whereas the intervening cortex flows towards the ring without expansion

To assess the significance of interactions between the contractile ring and surrounding cortex on contractile ring dynamics, we generated a 4D map of cortical flow to determine how the cortex responds to ring pulling. We monitored cortical movement at high time resolution (**Figure 1A, Video 1**) in embryos expressing a GFP fusion with the heavy chain of non-muscle myosin II (NMY-2; hereafter myosin::GFP; Figure 1 – Figure **Supplements 1, 2**), while also monitoring ring constriction at lower time resolution in the same embryos (**Figure 1A, Figure 1 – Figure Supplement 3**). Myosin::GFP flowed together with actin (LifeAct::mKate2) on the embryo surface (**Figure 1 – Figure Supplement 4)**, consistent with prior work indicating that the entire cell surface, from cortex-associated cytoplasmic granules to cell surface receptors, moves in a coordinated fashion during cytokinesis (Cao & Wang, 1990; DeBiasio, LaRocca, Post, & Taylor, 1996; Fishkind, Silverman, & Wang, 1996; Hird & White, 1993; Reymann et al., 2016; Swann & Mitchison, 1958; Wang, Silverman, & Cao, 1994). Because the contractile ring closes asymmetrically within the division plane ((Maddox, Lewellyn, Desai, & Oegema, 2007); **Figure 1A, Figure 1 – Figure Supplement 3**), the pattern of cortical movement cannot be inferred from imaging individual embryos. Therefore, we generated an average 4D map of cortical flow by computationally combining data from 93 embryos imaged in random rotational orientations (**Figure 1A, Figure 1 – Figure Supplement 3**). We defined the top of the embryo as the side where the furrow ingresses first, the bottom as the opposite side, and referenced positions around the embryo circumference by the angle θ. For temporal alignment, we fit a line to normalized ring size ($\bar{R} := R/R_{emb}$) versus time between 30% and 80% closure for each embryo, and extrapolated this line to 1 and 0 to define t_0 (cytokinesis onset) and t_{CK} (time of cytokinesis), respectively (**Figure 1A, Figure 1 – Figure Supplement 3**). Cortical flow could not be monitored in the division plane or at the cell poles, due to their high curvature. Thus, this approach provided a quantitative picture of cortical movement in the central 2/3 of the embryo throughout cytokinesis (**Figure 1B**; **Video 2**).

The 4D map of cortical flow allowed us to determine where new cortical surface is gained as the ring closes. New cortical surface could be gained uniformly, immediately behind the contractile ring, or at the cell poles (Bluemink & de Laat, 1973; Byers & Armstrong, 1986; Danilchik, Bedrick, Brown, & Ray, 2003; Gudejko, Alford, & Burgess, 2012; Selman & Perry, 1970; Swann & Mitchison, 1958; Turlier, Audoly, Prost, & Joanny, 2014; Zumdieck et al., 2007), with each pattern predicting a different profile of cortical velocity along the embryo axis (**Figure 1 – Figure Supplement 5**). The cortical velocity profiles measured from the flow map indicated that cortical surface is gained at the poles and subsequently moves with constant velocity towards the division plane (**Figure 1B**). The velocity of cortical flow was higher on the top of the embryo during the first half of cytokinesis when the furrow ingresses from the top (**Figure 1B, black traces**) and became higher on the bottom of the embryo towards the end when the furrow ingresses from the bottom (**Figure 1B, grey traces; Video 2**).

Cutting the cortex parallel or perpendicular to the division plane using a laser revealed that the cortex is under tension during cytokinesis (**Figure 2A**). However, parallel laser cuts had no effect on the constriction rate (**Figure 2B,C**) indicating that cortical tension does not impose significant resistance to ring pulling. Inhibiting the Arp2/3 complex by depleting its ARX-2 subunit, which is expected to reduce effective cortical viscosity and thus cortical tension (Chaudhuri, Parekh, & Fletcher, 2007; Davies et al., 2014; Tseng & Wirtz, 2004), also did not alter the constriction rate (**Figure 2 – Figure Supplement 1**). Together, these results indicate that the cortex at the poles expands in response to tension generated by the constricting ring, whereas the cortex in the region between the ring and the poles flows towards the ring without expansion or compression. This differential response of the polar cortex to ring-generated tension, which results in a flow of myosin and other cortical components towards the cell equator, is consistent with the idea of polar relaxation hypothesized in early conceptual models of cytokinesis (Greenspan, 1978; Swann & Mitchison, 1958; Taber, 1995; White & Borisy, 1983; Wolpert, 1960; Zinemanas & Nir, 1987, 1988).

The contractile ring pulls in extra cortex during constriction, leading to an exponential increase in the levels of ring components and in the ring constriction rate

Recent work in the *C. elegans* embryo suggested that recruitment of contractile ring proteins following anaphase onset leads to compression of the equatorial cortex that aligns actin filaments to form the contractile ring (Reymann et al., 2016). Consistent with this, a gradient of cortical flow velocity that spans the cell equator is observed in our flow map at early timepoints prior to furrow ingression (**Figure 2 – Figure Supplement 2**). After contractile ring assembly, the ring has been proposed to constrict in an autonomous manner via continuous disassembly (Murrell et al., 2015; Schroeder, 1975). In this view, the constricting ring would generate the division plane by pulling the cortex behind it, and the amount of cortex entering the division plane would equal the area of the division plane. To test this prediction, we analyzed the 4D cortical flow map to measure the total cortical surface area entering the division plane and compare it to the area of the division plane (accounting for the fact that two surfaces are generated-*red outline in* **Figure 3A**). Surprisingly, this analysis revealed that significantly more cortical surface entered the division plane than is necessary to build the plane: the flux of cortical area into the division plane was 1.5 to 2-fold higher than the rate of change in the area of the division plane throughout cytokinesis (**Figure 3A,B**). In control embryos, more cortex flowed in from the posterior side than from the anterior side, likely due to distinct mechanical cortical properties downstream of the polarity machinery. Consistent with this, and with prior work showing that Arp2/3 inhibition impairs the recruitment of PAR-2 to the posterior cortex and makes myosin and actin dynamics on the posterior cortex more similar to those in embryo anterior (Xiong, Mohler, & Soto, 2011), inhibiting the Arp2/3 complex by depleting ARX-2 abolished the difference between the two sides, but did not change the imbalance between the total amount of cortex entering the division plane and the area of the plane (**Figure 3 – Figure Supplement 1; Video 3**). Thus, significantly more cortical surface enters the division plane during cytokinesis than expected if the cortex passively trails behind the closing ring (**Figure 3A**).

The extra cortex delivered into the division plane could concentrate in the ring and contribute to its closure, distribute within the division plane, or be lost due to disassembly (**Figure 3C**). To distinguish between these and other possibilities, we monitored *in situ*-tagged myosin::GFP (Dickinson, Ward, Reiner, & Goldstein, 2013) (**Figure 3D**) and GFP::anillin (**Figure 3 – Figure Supplement 2**) in the division plane. Both probes exhibited similar behavior, accumulating primarily within the ring (**Figure 3D,**

Figure 3 – Figure Supplement 3). Quantification of mean per unit length fluorescence around the ring (after attenuation correction; **Figure 3 – Figure Supplement 4**) revealed a steady increase for both markers as constriction proceeded. The increase began on the top, which ingresses first, and initiated later on the bottom, which ingresses after the constriction midpoint (**Figure 3D, Figure 3 – Figure Supplement 3**). Thus, monitoring of myosin and anillin suggests that the extra cortical surface flowing into the division plane is incorporated into the ring and predicts that the amount of ring myosin and anillin should increase in proportion to the flux of extra cortical surface into the ring (**Figure 3E**). To test this prediction, we compared the per unit length rate of ring-directed cortical flow to the per unit length amounts of myosin and anillin. All were well-fit by the same single exponential (**Figure 3E,F**), consistent with the idea that cortical surface flowing into the division plane delivers components to the contractile ring during constriction.

The exponential increase in the per unit length levels of ring myosin and anillin during constriction (**Figure 3F**) is best explained by positive feedback: ring myosin pulls in adjacent cortex, bringing additional myosin motors into the ring that in turn increase the velocity of ring-directed cortical flow (**Figure 3G**). The per unit length constriction rate also increases with the same exponential kinetics as the per unit length rate of ring-directed cortical flow and the per unit length amounts of anillin and myosin (**Figure 3H**). This coupling likely arises because the constriction rate, like the rate of ring-directed cortical flow, depends on the amount of ring myosin. The exponential increase in the per unit length constriction rate explains the ability of contractile rings to close at a relatively constant rate despite their progressively decreasing perimeter (Biron et al., 2004; Bourdages et al., 2014; Calvert et al., 2011; Carvalho et al., 2009; Ma et al., 2012; Mabuchi, 1994; Pelham & Chang, 2002; Zumdieck et al., 2007). A relatively constant rate of closure is observed over a significant portion of ring constriction (**Figure 1A**; $t = 50$-200s) because the exponential increase in the per unit length constriction rate balances the decrease in ring size.

Component levels and fluorescence recovery after photobleaching of the division plane support constriction rate acceleration due to ring-directed flow versus component retention

Our results indicate that the per unit length amount of contractile ring components increases exponentially, and suggest that this increase is due to delivery by cortical flow along the direction perpendicular to the ring. In this model, constriction in the around-the-ring direction does not alter the per unit length amount of ring components, but instead drives ring disassembly that reduces the total amount of ring components in proportion to the reduction in ring length (**Figure 4A, left panel**). An alternative model for the increase in the per unit length amount of ring components, proposed based on work in fission yeast (Wu & Pollard, 2005), is that myosin and anillin could be retained within the ring rather than lost as ring perimeter decreases during constriction (**Figure 4A, middle panel**). In the retention model, the total amounts of both components remain constant as the ring closes resulting in an increase in their per unit length amount that is inversely proportional to the reduction in ring size. Comparison with the total amounts of ring myosin and anillin suggested that, whereas the retention model fits the data well for t/t_{ck} between 0.2 and 0.6, there was significant deviation for timepoints outside of this range. In contrast, the ring-directed cortical flow model fit the data for the entire measured interval (t/t_{ck}= 0.0 to 0.8; **Figure 4B, Figure 3 – Figure Supplement 3**).

To distinguish between the retention and ring-directed flow models using an independent approach, we photobleached myosin in the entire division plane at ~30% closure, and monitored its subsequent recovery in the ring (**Figure 4C**). The ring-directed cortical flow model predicts that the per unit length amount of bleached myosin should be constant and, since cortical myosin turns over faster than myosin in the ring ($t_{1/2}$ of ~30s (Mayer, Depken, Bois, Julicher, & Grill, 2010; Salbreux, Charras, & Paluch, 2012)), cortical flow should rapidly deliver unbleached fluorescent myosin to the ring, leading to an exponential increase comparable to that in controls. In contrast, the retention model predicts that the per unit length amount of bleached myosin and any residual fluorescent myosin that is retained in the ring will increase in proportion to the decrease in the ring size (~1/R). We found that the per unit length amount of fluorescent myosin in the ring increased exponentially following bleaching, and the difference between the control and the bleached embryos, which reflects the amount of bleached myosin, remained constant, both of which agree with the predictions of the ring-directed cortical flow model (**Figure 4C**). We note that this data also suggests that the recovery of myosin fluorescence in the ring in not due to exchange with myosin in the cytoplasm. If ring myosin were turning over due to exchange with cytoplasmic myosin, we would expect the FRAP curve to approach the control curve and the difference between the FRAP and control curves to disappear. Instead, the two curves remained parallel and the difference remained constant (**Figure 4C**). This data suggest that rather than being due to exchange with cytoplasmic myosin, the recovery of ring fluorescence is due to a mechanism in which myosin on the cortex adjacent to the ring turns over, allowing resumption of delivery of myosin to the ring by cortical flow.

The conclusion that the per unit length amount of contractile ring components increases exponentially during constriction is in apparent contradiction to analysis in 4-cell stage *C. elegans* embryos, where we had previously reported an ~1.3-fold increase in myosin, anillin and septins as the ring perimeter decreased 2-fold (from 50 to 25 μm). However, this is in fact consistent with the prediction of the ring-directed cortical flow model (see **Figure 4 – Figure Supplements 1, 2** for an analysis of ring component levels and recovery following photobleaching at the 4-cell stage).

Together these data suggest that, the acceleration of the per unit length constriction rate during closure, a conserved feature of contractile rings, does not arise from ring component retention, but from positive feedback between ring myosin and ring-directed cortical flow.

An analytical mathematical formulation for the positive feedback-mediated evolution of the contractile ring

The exponential accumulation of contractile ring components during constriction due to positive feedback means that the properties of the ring (component levels and constriction rate) are continuously changing. Thus, analysis of perturbations requires fitting temporal profiles of ring size or component levels and deriving meaningful quantitative parameters from these fits. In order to assess the consequences of molecular perturbations, we therefore translated our experimental findings (summarized in **Figure 5A**) into an analytical mathematical framework (see **Methods** for detailed derivation), consisting of three equations and three model parameters, that we named the Cortical Flow Feedback (CoFFee) model (**Figure 5B**). Based on our photobleaching data, we assume that: (1)

constriction in the around-the-ring direction does not alter the per unit length amount of ring components, but leads to ring disassembly that reduces the total amount of ring components in proportion to the reduction in ring length, and (2) myosin in the contractile ring does not turn over by exchange with myosin in the cytoplasm. Thus, increases in the per unit length amount of ring myosin are solely due to delivery by cortical flow along the direction perpendicular to the ring. We posit that myosin increases exponentially during constriction due to positive feedback between the per unit length amount of ring myosin and the velocity of cortical flow that delivers myosin into the ring. Positive feedback arises from the fact that the velocity of ring-directed cortical flow is proportional to the amount of ring myosin, and the amount of ring myosin increases in proportion to the velocity of cortical flow (**Figure 5A**). In our mathematical formulation, the velocity of ring-directed cortical flow ($v_{flow}(t)$) is related to the amount of ring myosin ($M_{ring}(t)$, per unit length) by a proportionality constant α that reflects the ability of the cortex to be compressed (**Figure 5B,** Eqn. (1)), and ring myosin increases at a rate proportional to the velocity of ring-directed cortical flow and the concentration of cortical myosin (m_{cort}; **Figure 5B**, Eqn. (2)). As a result of the positive feedback, ring myosin increases exponentially with a characteristic time $\tau \coloneqq 1/\alpha m_{cort}$ (time required for ring myosin to increase ~2.7 fold; **Figure 5B, lower left**). The per unit length constriction rate is proportional to the amount of ring myosin, being related by a constant β that reflects the ability of the ring to be constricted (**Figure 5B,** Eqn. (3)).

To obtain expressions for contractile ring size and component levels that can be used to fit data, we solved the model equations in a specific time reference. Instead of $t = 0$ being defined by extrapolation of plots of $\bar{R}$ $(\coloneqq R/R_{emb})$ versus time (**Figure 1A**), which is not ideal in a mathematical formulation, we set $t = 0$ as the halfway point of ring closure ($\bar{R}(t = 0) = \frac{1}{2}$). This time reference also avoids the difficulty of assessing cytokinesis onset. In this time reference, the equation for ring size is:

$$\bar{R}(\bar{t}\,) = \bar{R}_{ini}(2\bar{R}_{ini})^{-\exp(\bar{t}\,)}, \tag{4}$$

where $\bar{t} \coloneqq t/\tau$ and $\bar{R}_{ini}$ is the dimensionless characteristic ring size (held fixed at a value of 1.1; see Methods). Any component that localizes to the cell cortex will be delivered to the contractile ring via the same process as myosin, so contractile ring components all accumulate in a similar fashion, with

$$C_{ring}(\bar{t}\,) - C_{ring,base} = \frac{\alpha c_{cort}}{\beta}\ln(2\bar{R}_{ini})\,\mathrm{e}^{\bar{t}}, \tag{5}$$

$$C_{ring,base} := C_{0,ring} - \ln(2\bar{R}_{ini})\frac{\alpha c_{cort}}{\beta}, \tag{6}$$

where $C_{0,ring}$ is the per unit length amount of the component at the half-way point of ring closure, $C_{ring,base}$ is the baseline amount of the ring component that does not increase exponentially, and c_{cort} (m_{cort} for myosin) is the concentration of the component on the cortex that is delivered to the ring. The velocity of cortical flow and the constriction rate are

$$v_{flow}(\bar{t}\,) = \frac{\alpha}{\beta}\ln(2\bar{R}_{ini})\,\mathrm{e}^{\bar{t}}, \tag{7}$$

$$-\frac{1}{\bar{R}}\frac{d\bar{R}}{d\bar{t}} = \ln(2\bar{R}_{ini})\,\mathrm{e}^{\bar{t}}. \tag{8}$$

Thus, the per unit length constriction rate, velocity of cortical flow, and ring component amounts all increase exponentially with the characteristic time of ring myosin accumulation ($\tau = 1/\alpha m_{cort}$) set by the feedback loop between ring myosin and cortical flow (**Figure 5B**), as we observe experimentally (**Figure 3E-H**).

Reducing the concentration of cortical myosin reduces the ability of the ring to be constricted by ring myosin

To address the effect of reducing myosin activation on cytokinesis, we used our mathematical formulation to analyze the effects of depleting rho kinase (LET-502). Rho kinase contributes to myosin activation by promoting regulatory light chain phosphorylation. Due to parallel pathways for myosin activation, penetrant rho kinase inhibition slows, but does not prevent, ring constriction (Maddox et al., 2007; Matsumura, 2005; A. J. Piekny & Mains, 2002). We imaged control and rho kinase-depleted embryos expressing *in situ* tagged myosin::GFP. To assess the impact of rho kinase inhibition on the properties of the ring and cortex encoded in our three model parameters (α, β, and m_{cort}), we directly measured m_{cort} and fit experimental measurements of ring size and ring myosin versus time to equations (4) and (5) to determine the effects on α and β (**Figure 6A**). Direct measurement revealed that the amount of cortical myosin, m_{cort}, was reduced by 20% in rho kinase depleted embryos compared to controls ($m_{cort}^{RKdep} = 0.8\, m_{cort}^{WT}$; **Figure 6B**). Next, we fit traces of ring size versus time using the ring size equation (4) to determine characteristic times, ($\tau = 1/\alpha m_{cort}$), for each embryo. This analysis revealed that τ was 1.3-fold higher in rho kinase-depleted embryos compared to controls (120 ± 20 s versus 90 ± 10 s in controls; **Figure 6C, middle row**) indicating that $\alpha^{RKdep}\, m_{cort}^{RKdep} = 0.8\, \alpha^{WT}\, m_{cort}^{WT}$. Since $m_{cort}^{RKdep} = 0.8\, m_{cort}^{WT}$, we conclude that $\alpha^{RKdep} = \alpha^{WT}$; thus, the ability of the cortex to be compressed by ring myosin is not affected by rho kinase depletion. To determine the effect on β, we measured the mean per unit length amount of myosin::GFP in the ring versus time in control and rho kinase depleted embryos and fit the data to the equation for ring myosin (5). Interestingly, the per unit length amount of myosin for a given ring size was the same in control and rho kinase depleted embryos, resulting in an equivalent exponential prefactor for the two conditions ($\alpha^{RKdep}\, m_{cort}^{RKdep}/\beta^{RKdep} = \alpha^{WT}\, m_{cort}^{WTp}/\beta^{WT}$; **Figure 6C, bottom row, Figure 6 – Figure Supplement 1**). From this we conclude that the ability of the ring to be constricted by ring myosin is reduced in rho kinase depleted embryos compared to controls ($\beta^{RKdep} = 0.8\, \beta^{WT}$).

The effects of rho kinase inhibition identified by our analysis are schematically summarized in Figures 7A and B. Rho kinase inhibition decreases the concentration of cortical myosin, m_{cort} , to 80% of its value in controls, which slows myosin accumulation via the feedback loop and increases τ. Normalizing time by τ and setting $\bar{t} = 0$ at 50% closure superimposes the constriction rate curve with the control (**Figure 7B, Figure 7 – Figure Supplement 1**). This is a convenient reference frame for comparing two conditions because comparing component levels and flow velocity at the same $\bar{t}$ corresponds to comparing them for the same ring size. Perturbations that reduce the ability of the ring to be constricted by ring myosin (reduce β) introduce a time delay between cortical flow/accumulation of contractile ring components and the constriction rate (see **Figure 7 – Figure Supplement 2** for detailed explanation). The length of the delay is the amount of time it takes for the feedback loop to accumulate enough ring myosin to compensate for the reduction in β. After the delay, ring closure proceeds with kinetics identical to controls but with higher flow velocities and ring component concentrations. Due to the reduction in β in rho kinase depleted embryos, the velocity of cortical flow is predicted to be 1.25 fold higher for all ring sizes in the $\bar{t}$ reference frame (**Figure 7B**, middle panel). Thus, our analysis suggests that the per unit length amount of myosin is the same for rings of all sizes in control and rho kinase depleted embryos (**Figure 6C**) because there is an increase in the amount of cortical flow into the ring that compensates for the reduction in the concentration of cortical myosin (**Figure 7B**, last panel).

Filming control and rho kinase depleted embryos expressing GFP::anillin and measuring the concentration of cortical anillin ($c_{ani,cort}$) revealed that it is not altered by rho kinase inhibition. Thus, if our prediction that there is more cortical flow into the ring in rho kinase depleted embryos is correct, the per unit length amount of cortical anillin should be 1.25-fold higher in rings of all sizes in rho kinase depleted embryos compared to control embryos. Consistent with this prediction, measurement of mean per unit length GFP::anillin fluorescence in the ring revealed a 1.21 fold increase (**Figure 7C, Figure 6 – Figure Supplement 1**). Thus, an analysis of rho kinase-depleted embryos employing the mathematical formulation of the positive feedback model for cytokinetic ring closure leads to the counterintuitive conclusion that reducing the concentration of cortical myosin makes it more difficult for rings of the same size with the same amount of myosin to constrict. We suggest that this may be because the compensatory increase in cortical flow that restores ring myosin to control levels leads to an overabundance of other components (e.g. anillin) that increase resistance of the ring to constriction. More broadly, the analysis of rho kinase inhibition, employing straightforward-to-measure experimental parameters, highlights the utility of the mathematical formulation we present to explain the complex and non-intuitive effects of molecular perturbations on cytokinesis.

DISCUSSION

Despite the physical connection between the contractile ring and adjacent cortex, how these interconnected regions function together to change cell shape during cytokinesis has not been clear. Here, we explore this question during the first division of the *C. elegans* embryo by generating a 4D map of cortical flow in conjunction with laser ablation experiments and monitoring of ring component dynamics in the division plane. Our results indicate that polar relaxation collaborates with cortical contractility at the cell equator to enable the assembly and subsequent structural evolution during constriction of the contractile ring. In particular, we show that the pattern of polar relaxation and equatorial contractility set up by spindle-based signaling generates a positive feedback loop between ring myosin and ring-directed cortical flow that feeds the ring. The resulting exponential increase in the per unit length constriction rate explains the ability of the ring to close at a relatively constant overall rate despite its progressively decreasing perimeter during constriction. The broad conservation of this property (Biron et al., 2004; Bourdages et al., 2014; Calvert et al., 2011; Carvalho et al., 2009; Ma et al., 2012; Mabuchi, 1994; Pelham & Chang, 2002; Zumdieck et al., 2007), which allows cytokinesis to complete in a temporally restricted cell cycle window (Canman et al., 2000; Martineau et al., 1995; Straight et al., 2003), suggests that feedback between contractile ring myosin and ring-directed cortical flow will be a broadly conserved property of contractile rings in animal cells. The feedback-based mechanism we describe here, in which the increase in myosin levels in the ring is due to cortical flow along the direction perpendicular to the ring contrasts with prior models, including a model previously proposed by our group, that constriction rate acceleration arises from the ring-intrinsic retention of force generating units (Carvalho et al., 2009; Wu & Pollard, 2005).

In addition to ensuring timely cell content partitioning, the feedback-based mechanism that we describe renders the ring robust to defects in the cytokinesis machinery that increase the difficulty of ring constriction, such as in the inhibition of rho kinase that we investigate here, and/or to internal or external mechanical challenges, such as cell-cell contacts or obstacles in the crowded cell interior. In all of these cases, the feedback loop between ring myosin and cortical flow would lead to the progressive build up of contractile ring components until constriction proceeded. An interesting caveat, suggested by modeling

(**Figure 7—figure supplement 2**) is that molecular perturbations that reduce the ability of the ring to be constricted by ring myosin (reduce β in the mathematical formulation) do not alter the kinetics of contractile ring closure. Instead, they introduce a time delay that allows the ring to accumulate enough myosin to overcome the reduced β. After this delay, constriction proceeds with kinetics identical to controls, but with higher component levels and flow velocities throughout closure. Experimentally, this means that perturbations that make ring constriction more difficult will not be detected by monitoring constriction kinetics in the absence of a reliable time reference for cytokinesis onset, since the introduced delay may be relatively small. The second signature feature of these perturbations, higher component levels throughout closure, would likely be easier to measure (e.g., by quantifying ring component levels at the closure halfpoint).

We note that ring-directed flows have also been observed in the context of wound healing (Mandato & Bement, 2003), and similar types of cortical dynamics driven by coordinated patterns of contractility and relaxation are relevant in many contexts including cell polarization, cell motility, and tissue morphogenesis (Gardel, Schneider, Aratyn-Schaus, & Waterman, 2010; Munjal & Lecuit, 2014; Salbreux et al., 2012), suggesting that the positive feedback between myosin in contractile structures and cortical flow will act in physiological contexts beyond cytokinesis.

Polar relaxation enables ring-directed cortical flow that feeds the contractile ring during constriction

The cortical flow map and laser ablation analysis indicate that recruitment of myosin to the equatorial cortex leads to local compression that places the adjacent cortex under tension. In response to this tension, the polar cortex expands; in contrast, the cortex between the poles and the equator flows towards the ring without expanding. These observations suggest that the polar cortex has distinct mechanical properties. These distinct properties could arise from different, non-exclusive mechanisms. The polar cortex may be less stiff than the rest of the cortex, causing it to stretch and thin in response to ring constriction-induced tension. Consistent with this idea, a reduction in f-actin intensity at the cell poles has been reported during cytokinesis in *Drosophila* cells due to delivery of a phosphatase by segregating chromosomes (Rodrigues et al., 2015). Alternatively, the polar cortex may turnover more rapidly, leading to a higher rate of surface renewal after stretching. A third possibility is that the polar cortex is more prone to rupture, repair of which would locally increase cortical surface. Consistent with this last idea, blebs have been reported at the cell poles in cultured vertebrate and *Drosophila* cells, where they have been proposed allow cells to elongate in anaphase and release tension at the poles (Hickson, Echard, & O'Farrell, 2006; Sedzinski et al., 2011). Understanding precisely how the polar cortex is different in molecular and mechanical terms, and the mechanisms that generate these differences are important goals for future work.

Early conceptual models of cytokinesis hypothesized that polar relaxation coupled to a global upregulation of surface tension could trigger a flow of tension-generating elements towards the equator that would compress into a circular band and initiate a feedback loop similar to the one we describe here (Greenspan, 1978; Swann & Mitchison, 1958; Taber, 1995; White & Borisy, 1983; Wolpert, 1960; Zinemanas & Nir, 1987, 1988). Although polar relaxation could drive cytokinesis on its own, the compressed band of cortex would be sensitive to the mechanical properties of the cortex and the amount and timing of relaxation at each pole. Any non-uniformity, for example due to cell-cell contacts, could lead to unstable positioning or collapse of the ring to one side (Greenspan, 1978). Similarly, mechanisms that promote cortical contractility at the cell equator could initiate ingression; however, in the absence of cortical relaxation, cytokinesis would stall due to progressively increasing cortical tension. Coupling equatorial contractility to polar relaxation, as we observe in the *C. elegans* embryo, has two beneficial effects: (1) it releases the isotropic tension produced by compression of the equatorial cortex along the direction perpendicular to the ring, leading to filament alignment and ring narrowing that reduces resistance from cytoplasmic pressure and, (2) it allows the ring to establish a pattern of ring-directed cortical flow to generate a feedback loop that provides components to the ring in proportion to the velocity of cortical flow rather than the rate of network turnover.

Information on constriction kinetics and patterning of cortical compression/expansion suggests that a similar coupling may also support ring constriction in sea urchin embryos. Cleaving sea urchin embryos from a variety of species exhibit constriction kinetics essentially identical to those during the first division of the *C. elegans* embryo (Mabuchi, 1994). Pioneering work by Katsuma Dan monitoring surface expansion and compression by measuring the distance between surface-adhered particles and the distribution of pigmented cortex-associated granules (Dan, 1954; Dan & Dan, 1940; Dan, Dan, & Yanagita, 1938), suggests that sea urchin embryos also exhibit patterned relaxation during ring constriction. However, rather than being confined to the pole as it is in the *C. elegans* embryo, compression of the equatorial cortex is coupled to a wave of cortical expansion that initiates at the poles and propagates through to the region adjacent to the furrow (Dan et al., 1938; Dan & Ono, 1954; Dan, Yanagita, & Sugiyama, 1937; Swann & Mitchison, 1958), a result recently confirmed by experiments employing a probe that binds lipid rafts (Gudejko et al., 2012). Cortical compression and expansion have not been mapped in vertebrate cells; however, monitoring of fluorescent latex spheres adhered to cell surface proteins (Fishkind et al., 1996; Wang et al., 1994), injected stabilized fluorescent actin filaments (Cao & Wang, 1990), and fluorescently labeled myosin II (DeBiasio et al., 1996) have all revealed concerted cortical flow towards the division plane in the equatorial region of the cell that contrasted with random surface movements at the cell poles, suggesting a pattern similar to the one we describe here for the *C. elegans* embryo.

The CoFFee model as a tool to dissect the consequences of molecular perturbations

The ability to analyze the effects of mutations and other molecular perturbations is essential to defining molecular mechanisms. The exponential accumulation of contractile ring components during constriction due to positive feedback means that the properties of the ring (component levels and constriction rate) are continuously changing. The existence of the feedback loop can also to somewhat counterintuitive results—for example, perturbations that increase the difficulty of ring constriction delay constriction onset rather than slowing constriction kinetics. Deconvolving the phenotypes observed following specific perturbations therefore poses a significant challenge. To address this challenge, we generated a straightforward analytical mathematical formulation (the CoFFee model) consisting of three differential equations and three parameters that reflect the empirical properties of the ring and cortex. In addition to describing the processes underlying the evolution of the contractile ring, the CoFFee model provides a simple framework for analyzing experimental data. As we demonstrate here for rho kinase depletion, assessing the effects of a perturbation on model parameters provides insights into the underlying mechanistic effects of the perturbation. For example, the analysis of rho kinase depleted embryos suggests that reducing the concentration of cortical myosin leads to a compensatory increase in cortical flow that restores ring myosin to control levels—we note that the reason for this compensation is a fascinating topic for future work. Since the CoFFee model encapsulates experimental data to accurately describe the dynamics of the contractile ring and associated cortical network, an additional interesting future direction will be to use parameter changes derived from the CoFFee model as input for a finite-element model (similar to (Turlier et al., 2014)) in order to predict the evolution of cell shape given an *a priori* knowledge of cortical and contractile ring dynamics.

METHODS

C. elegans strains used in this study

Strain Name	Genotype	Reference
OD821	*ltSi200[pOD1997; Pnmy-2::nmy-2::gfp; cb-unc-119(+)] II; unc-119(ed3) III*	This study
OD857	*ltSi200[pOD1997; Pnmy-2::nmy-2::gfp; cb-unc-119(+)] II; unc-119(ed3); ruIs32[pAZ132; pie-1/GFP::histone H2B] III*	This study
OD858	*ltSi803[pOD1998; Parx-7::GFP::arx-7; cb-unc-119(+)] II; unc-119(ed3) III;*	This study
LP162	*nmy-2(cp13[nmy-2::gfp + LoxP]) I*	(Dickinson et al., 2013)
OD95	*unc-119(ed3) III; ltIs37 [pAA64; Ppie-1::mCherry::his-58; unc-119(+)] IV; ltIs38 [pAA1; Ppie-1::GFP::PH(PLC1delta1); unc-119 (+)]*	(Essex, Dammermann, Lewellyn, Oegema, & Desai, 2009)
OD3011	*ltSi1123[pSG017; Pani-1::GFP::ani-1 RE-encoded-exon5::ani-1 3'-UTR; cb unc-119(+)]II;unc-119(ed3)III*	This study
GOU2047	*cas607[arx-2::gfp knock-in] V*	(Zhu et al., 2016)

The *C. elegans* strains listed in the table were maintained at 20°C using standard methods. OD821 and OD858, expressing NMY-2::GFP, GFP::anillin, and GFP::ARX-7 were generated using a transposon-based strategy (MosSCI; (Frokjaer-Jensen et al., 2008)). Genomic regions encoding *nmy-2* (including 2079 bp and 1317 bp up and downstream of the stop codon, respectively), *ani-1* (including 2015 bp and 1215 bp up and downstream of the stop codon), and *arx-7* (including 3056 bp and 634 bp up and downstream of the stop codon) were cloned into pCFJ151 and sequences encoding GFP were inserted either just before (*nmy-2*) or after (*arx-7* and *ani-1*) the start codon. The single copy *nmy-2* transgene was generated by injecting a mixture of repairing plasmid (pOD1997, 50ng/µL), transposase plasmid (pJL43.1, Pglh-2::Mos2 transposase, 50ng/µL), and fluorescence selection markers (pGH8, Prab-3::mCherry neuronal, 10ng/µL; pCFJ90, Pmyo-2::mCherry pharyngeal, 2.5ng/µL; pCFJ104, Pmyo-3::mCherry body wall, 5ng/µL) into EG6429 (ttTi5605, Chr II). Single copy *ani-1* and *arx-7* transgenes were generated by injecting a mixture of repairing plasmid (pSG017 (*ani-1*) or pOD1998 (*arx-7*), 50ng/µL), transposase plasmid (CFJ601, Peft-3::Mos1 transposase, 50ng/µL), selection markers (same as for *nmy-2* strain) and an additional negative selection marker (pMA122; Phsp-16.41::peel-1, 10ng/µL) into EG6429 (ttTi5605, Chr II). After one week, progeny of injected worms were heat-shocked at 34°C for 2-4 hours to induce PEEL-1 expression and kill extra chromosomal array containing worms (Seidel et al., 2011). Moving worms without fluorescent markers were identified and transgene integration was confirmed in their progeny by PCR spanning both homology regions in all strains.

C. elegans *RNA-mediated interference*

Gene	**Oligonucleotide 1**	**Oligonucleotide 2**	**Template**	**mg/ ml**
arx-2 (K07C5.1)	TAATACGACTCACTATAGGTCAGCTTCGTCAAATGCTTG	AATTAACCCTCACTAAAGGTGCAATACGCGATCCAAATA	N2 DNA	1.7
let-502 (C10H11.9)	TAATACGACTCACTATAGGCAGCGATCGTCTGCTTATCA	AATTAACCCTCACTAAAGGTGGCTGTCGAGTTACGAATG	N2 DNA	1.9

Single-stranded RNAs (ssRNAs) were synthesized in 50μL T3 and T7 reactions (MEGAscript, Invitrogen, Carlsbad, CA) using cleaned DNA templates generated by PCR from N2 DNA using the oligos in the table above. Reactions were cleaned using the MEGAclear kit (Invitrogen, Carlsbad, CA), and the 50 μL T3 and T7 reactions were mixed with 50μL of 3× soaking buffer (32.7mM Na_2HPO_4, 16.5mM KH_2PO_4, 6.3mM NaCl, 14.1mM NH_4Cl), denatured at 68°C for 10min, and then annealed at 37°C for 30 min to generate dsRNA. L4 hermaphrodite worms were injected with dsRNA and allowed to recover at 16°C for 44-50 hours prior to imaging.

Monitoring cortical flow

Cortical flow was monitored in images of the cortical surface in embryos expressing myosin::GFP obtained from adult hermaphrodites by dissection. Embryos were mounted followed by sealing with a coverslip on double thick (1 mm) low percentage agarose (0.5%) pads to prevent compression that biases the initial angle of furrow ingression (**Figure 1 – Figure Supplement 2**). Images were acquired on an inverted microscope (Axio Observer.Z1; Carl Zeiss) equipped with a spinning-disk confocal head (CSU-X1; Yokogawa) and a 63× 1.40 NA Plan Apochromat lens (Zeiss) using a Hamamatsu Orca-ER digital camera (Model C4742-95-12ERG, Hamamatsu photonics). Images were collected using custom software, written in Python, that utilizes the Micro-Manager (open source software, (Edelstein et al., 2014)) microscope control library. A 3 x 0.75 μm z-series was collected (400ms exposure, 10-20% laser power) every 2s. After 15 time points, a 15 x 1μm z-stack, offset by 3μm from the cortical surface, was imaged to monitor the position of the closing contractile ring. The entire imaging series was repeated every 36s until the end of cytokinesis. Cortical flow was measured in maximum intensity projections of the 3 x 0.75μm z-stacks of the cortical surface, after orientation of the images to place the embryo anterior at the top and the posterior at the bottom, by correlating myosin fluorescence between consecutive images using Gunnar Farnebäck's algorithm (Farnebäck, 2003) implemented within the openCV library with a 30-pixel window size. The threshold was calculated for every image by maximizing the ratio of total intensity inside a 200x350 pixel box positioned in the center of the embryo to the total intensity outside that box.

Measurement of contractile ring position and size

Automated methods were employed to identify the edges of the embryo, determine the position of the contractile ring, and reconstruct the rings for each time point in an end-on view to determine the initial ingression axis (**Figure 1 – Figure Supplement 3**). Ring size and position were determined using custom Python software that: (1) identifies the orientation of the anterior-posterior (AP) axis and rotates the embryo to place the embryo anterior at the top and the embryo posterior at the bottom, (2) finds the embryo center in different x-z planes along the AP axis and calculates embryo radius, and (3) calculates the radius of the contractile ring and determines its position within the division plane. Details of each step are outlined below.

<u>Orienting embryos with their anterior end to the top:</u> Acquired z-plane images were convolved with a 10-pixel Gaussian kernel to reduce noise. An optimal signal threshold that partitioned the embryo interior from exterior was identified by finding a local minimum in the intensity histogram that produced a binary mask with expected area (~120000±50000 pixel^2). The orientation of the AP axis was identified by fitting an ellipse to the thresholded area in the middle plane of the z stack. The anterior side was identified by higher cortical myosin fluorescence and all images were rotated to place the embryo anterior at the top of the image and the embryo posterior at the bottom.

Defining the central axis of embryo and determining embryo width: The central axis of the embryo was defined by drawing a horizontal line across the oriented embryo at the midpoint between its anterior and posterior ends and identifying the first and last points along this line with signal above the threshold for each z-plane. The identified pixels were virtually projected in an end-on (x-z) view and fit to a circle by minimizing residuals. To account for fluctuations in the embryo boundary due to noise and fluorescence variation, the procedure was repeated 9 more times after shifting the position of the horizontal line towards the anterior pole by 10 pixels, covering approximately 1/5 of the embryo length (500 pixels). The position of the AP axis and the radius of the embryo were determined by averaging the 10 measurements.

Measuring contractile ring size and position: As illustrated for the central plane images shown in Figure 1 – Figure Supplement 3, the position of the contractile ring was determined by identifying pairs of points with the highest myosin fluorescence intensity on the opposite edges of the embryo in each z-plane that were not more than 20 pixels apart in the horizontal direction and were located at a y-axis position near the embryo middle. Contractile ring radius and position were determined by projecting the points to generate an end-on (x-z) view and fitting the data with a circle. The ring fit was iteratively improved by calculating predicted positions of myosin fluorescence at the ring in each z-plane using initially fitted parameters. Intensity maxima within 5 pixels of the predicted location were identified and the ring was refit. The initial guesses for the contractile ring size and position at the next time point were estimated from the previously calculated ring values. The algorithm restricted ring position fluctuations to 20 pixels along anterior-posterior axis and the size was estimated assuming constant rate of ring constriction. The automatic ring measurements were manually confirmed for each embryo. The initial ingression axis was determined as illustrated (**Figure 1 – Figure Supplement 3**) by fitting a line through the centers of the rings with a normalized ring size ($\bar{R} := R/R_{emb}$) > 0.3.

Embryo time alignment for averaging

Sequences from individual embryos were time aligned by defining zero time (t_0) and the total time of cytokinesis (t_{CK}) for each embryo, and normalizing time by t_{CK} prior to averaging, $\hat{t} \coloneqq \frac{t-t_0}{t_{CK}}$. An initial determination of t_0 and t_{CK} was made by fitting a line to the plot of normalized ring size ($\bar{R}(t) \coloneqq R/R_{emb}$) versus time between 30% and 80% closure for each embryo as outlined in Figure 1a. Extrapolation of this line for each embryo defined t_0 as the time where the fitted line intersects 1, and the time of cytokinesis, t_{CK} as the time where the fitted line intersects 0. Due to the small number of measurements from each embryo available for fitting (3-5 values where 0.8> $\bar{R}$ >0.3), the values of t_0 and t_{CK} were refined by fitting $\bar{R}(\hat{t})$ for each embryo to the average dimensionless ring size, $<\bar{R}>(\hat{t})$. Calculation of the average dimensionless ring size was performed in iterative manner. The time for each embryo was aligned by t_0 and normalized by t_{CK} using estimates from the fitted line in the first iteration. The average dimensionless ring size ($<\bar{R}>(\hat{t})$) was calculated by averaging normalized ring sizes of all embryos at corresponding normalized time. Contractile ring size was approximated for intermediate time points by linear interpolation. In further iterations, t_0 and t_{CK} were refined for every embryo by minimizing the residuals between its normalized ring size, $\bar{R}(\hat{t})$, and the average dimensionless ring size, $<\bar{R}>(\hat{t})$, throughout the entire timecourse of cytokinesis, thus increasing the number of time points available for fitting t_0 and t_{CK} (6-10 values per embryo). After refining time alignment and normalization for each embryo, average dimensionless ring size was re-calculated and t_0 and t_{CK} were refined for each embryo again. The refinement process was repeated until changes in average dimensionless ring size, $<\bar{R}>(\hat{t})$, were smaller than 0.001 on average (achieved within a few iterations). The collective fitting of all t_0 and t_{CK} at every iteration was performed under restriction that the line fit through $<\bar{R}>(\hat{t})$ between 0.8 and 0.3 intercepted 0 at $\hat{t}=0$ and 1 at $\hat{t}=1$. This restriction ensured that t_0 and t_{CK} determined from fits of individual embryos to the average ring size would be consistent with their original definition. The dimensional ring kinetics, $<R>(t)$, can be recovered using the following equation

$$<R>(t) = <R_{emb}><\bar{R}>(\hat{t}<t_{CK}>), \tag{9}$$

where $<R_{emb}> = 14.7 \pm 0.7\ \mu m$ and $<t_{CK}> = 200 \pm 30\ s$ are average embryo radius and time of cytokinesis accordingly.

Cortical flow averaging

Cortical flow averaging was performed after spatial and temporal alignment of data collected in different embryos (n=93 embryos from 93 worms filmed over the course of 5 days for control, **Video 2**; n=68 embryos from 68 worms filmed over the course of 4 days for *arx-2(RNAi)*, **Video 3**). The number of embryos was chosen to achieve at least 10-fold coverage for all areas of the cortical map for controls and 5-fold coverage for *arx-2(RNAi)*. Linear interpolation was used to approximate the flow between consecutive time points. Because our imaging regime required periodic z-stack acquisition to determine the trajectory of ring closure, no flow approximation was done during those time periods (~6s gap every 30s). The flow data for each time point was represented as a set of vectors with direction and magnitude corresponding to the direction and magnitude of the cortical flow at the base of the vector. The base of each vector had two spatial coordinates: x, the position along the anterior-posterior axis (where the position of the contractile ring was defined as 0), and θ, the angular position relative to the initial ingression axis (defined as described in **Figure 1A and Figure 1 – Figure Supplement 3**). We note that mitotic exit is accompanied by a brief (~50-60s) period of rotational flow ((Naganathan, Furthauer, Nishikawa, Julicher, & Grill, 2014; Schonegg, Hyman, & Wood, 2014); see **Video 1;**), which dissipates soon after initiation of cytokinesis (~$\hat{t}$=0.2-0.3). As this rotational contribution is not relevant here, we removed it by averaging the data from the right and left halves of the embryo (in an end-on view), allowing us to focus on rotation-independent flows. Thus the flow with angular positions greater than 180 degrees was mirrored in angular direction

$$f_{\theta}(\hat{t}, x, \theta > 180) \ \rightarrow -f_{\theta}(\hat{t}, x, 360 - \theta), \tag{10}$$

f_{θ} is the angular component of the flow vector $\vec{f}$. The flows were normalized by the embryo size and cytokinesis rate $\vec{\bar{f}}(\hat{t}, x, \theta) \coloneqq \frac{t_{CK}}{R_{emb}} \vec{f}(\hat{t}, x, \theta)$ and averaged according to its position and time

$$< \vec{\bar{f}} > (\hat{t}, x, \theta) = \frac{\sum_{emb} \vec{\bar{f}}(\hat{t}, x, \theta)}{N_{emb}}. \tag{11}$$

Calculation of expected cortical surface flow profiles

To aid in the interpretation of experimental results, expected profiles for cortical surface movement were calculated for defined patterns of cortical surface increase and plotted (**Figure 1B and Figure 1 – Figure Supplement 5**). The general form of surface movement velocity is given by the following equation

$$v(x) = \int_0^x g(x')dx' + u, \qquad (12)$$

where $g(x)$ is the amount surface gain and u is the velocity of asymmetric ring movement, which could be positive or negative, depending on whether the ring is moving towards or away from the surface. From equation (12) we obtain the following predictions

Uniform surface increase: $v(x) = Cx + u$;

Polar surface increase: $v(x) = C + u$;

Behind the ring surface increase: $v(x) = u$ (if the asymmetry of cytokinetic furrowing arises due to global surface movement) or $v(x) = 0$ (if the asymmetry in surface increase is related to the asymmetric furrowing).

Cortical laser ablation

Cortical laser ablations, presented in Figure 2, were performed using a robotic laser microscope system (RoboLase) (Botvinick & Berns, 2005). Embryos expressing myosin::GFP were mounted using standard procedures. A cortical cut, approximately 10 μm long, was made on the anterior side of the embryo when the ring was at ~50% closure (7μm radius). The cut was confirmed by comparison of cortical fluorescence images before and after the cut and was considered successful if the foci moved away from the cut area (~3.5μm distance), indicating cortical tension release. Contractile ring closure rate was calculated by measuring the difference in ring sizes before and after the cut, assessed from two 4x2μm z-stacks acquired immediately before the cut and 13s later. Errors in measuring the radius at the two timepoints were determined from the procedure used to fit the data to a circle and were propagated to determine the errors in the constriction rate measurements for individual embryos; mean errors are S.E.M. The cortical opening after ablation was approximately 35μm^2; this translates into an additional reduction in ring radius by ~0.8μm, if the cortical surface tension dominates the ring closure rate. This additional decrease in ring size within 13s should correspond to increase of the control rate (0.22μm/s) by ~30% (0.06µm/s). The experiment was repeated 19 times for no cut condition, 14 times for parallel cut, and 15 times for perpendicular cut. All imaging was performed over the course of 5 days. The number of embryos was chosen to achieve sufficient accuracy in the determination of mean ring closure rates to assess whether it was altered by the cuts.

Calculation of the surface area flowing into the division plane

We calculated the amount of surface area flowing into the division plane from flow measurements made 7 µm away from the position of the furrow on the anterior and posterior sides (as illustrated in **Figure 3A**). The rate of the surface flow is

$$\frac{dA_{surf}}{d\hat{t}}(\hat{t}) = 2R_{emb}\int_0^{\pi} < \vec{f} > (\hat{t}, x_0, \theta)d\theta \ , \tag{13}$$

where x_0 is -7 µm and 7 µm for the rate of flow from the anterior or the posterior sides, respectively. The total amount of surface area that entered the division plane from any time $\bar{t}_0$ to $\bar{t}$ is obtained by integrating equation (13) over time

$$A_{surf}(\hat{t}) = \int_{\hat{t}_0}^{\hat{t}} \frac{dA_{surf}}{d\hat{t}}\bigg|_{ant} + \frac{dA_{surf}}{d\hat{t}}\bigg|_{post}(t')dt'. \tag{14}$$

The increase in area of the division plane was calculated as following

$$A_{div\ plane}(\hat{t}) = 2\pi(< R >^2 (\hat{t}_0) - < R >^2 (\hat{t})). \tag{15}$$

In Figure 3A we used $\hat{t}_0 = -0.2$. The extra cortex delivered into the ring can be inferred from the difference between the surface area entering the division plane and the area of the division plane

$$A_{flow}(\hat{t}) := A_{surf}(\hat{t}) - A_{div\ plane}(\hat{t}). \tag{16}$$

Division plane imaging

For quantification of myosin::GFP and GFP::anillin amounts in the contractile ring, adult worm dissection and one-cell stage embryos imaging was performed in a custom microdevice (Carvalho et al., 2011). The device was mounted on an inverted microscope (Axio Observer.Z1; Carl Zeiss) and embryos were imaged with a 63x1.4NA Plan Apochromat objective using an electron-multiplying charge-coupled device camera (QuantEM:512SC, Photometrics; 100ms exposure, EM gain set to 500, 10% laser power). Division planes were reconstructed from 40 x 0.5μm z-stacks collected every 30s after background subtraction and attenuation correction. All imaging was done at 20°C.

Contractile ring photo-bleaching and imaging

1-cell stage embryos were mounted in microdevices as for division plane imaging and 4-cell stage embryos were mounted on slides with 2% agarose pads. Embryos were imaged on a Nikon TE2000-E inverted microscope equipped with a 60x1.40NA objective, an EM-CCD camera (iXon; Andor Technology; EM-Gain=220, Exposure =100ms), and a krypton-argon 2.5 W water-cooled laser. For 1-cell stage embryos, division planes were reconstructed from 30x1μm stacks acquired every 20s with 20% laser power and photo-bleaching was performed by 2 sweeps of a 488nm laser with 100% power and 500μs dwell time. For 4-cell stage embryos, division planes were reconstructed from 16x1μm stacks acquired every 10s with 50% laser power and photo-bleaching was performed by 2 sweeps of a 488nm laser with 100% power and 100μs dwell time. For 4-cell stage embryos, the time between the prebleached and first postbleached images was 6s.

Estimation of depth attenuation

To estimate depth attenuation within the division plane, we quantified the intensity of the division plane in two cell embryos expressing a GFP-tagged probe expected to be uniformly present on the plasma membrane. From each image, we subtracted a background intensity calculated as the average value inside two 4x4 μm rectangles positioned 2 μm away from the division plane inside the anterior and posterior cells. The division plane intensity profile was obtained by performing a 30 pixel maximum intensity projection along the AP axis, with the division plane positioned approximately in the middle (**Figure 3 – Figure Supplement 4**). The intensity profiles in z from 13 embryos were fitted to an exponential using the same characteristic attenuation depth for all embryos

$$I = I_0 e^{-z/z_{att}}, \tag{17}$$

which yielded a characteristic depth of attenuation, z_{att}, of 15 μm.

Quantification of myosin and anillin intensity in the contractile ring and on the cortex

For embryos at the 1-cell stage, myosin::GFP and GFP::anillin intensities in the contractile ring and on the cortex were quantified in 40x0.5 μm z-stacks containing the ring after correction for depth attenuation and subtraction of background fluorescence. Average intensity along the ring was calculated across a set of embryos in 30 degree arcs (for myosin::GFP, n=36 embryos from 18 worms filmed over 5 days for controls and 24 embryos from 15 worms filmed over 5 days for *let-502(RNAi)*; for anillin::GFP, n= 26 embryos from 14 worms filmed over 4 days and 30 embryos from 18 worms filmed over the course of 4 days for *let-502(RNAi)*). The number of embryos was chosen to determine mean fluorescence with sufficient accuracy to derive appropriate conclusions. Positions along the ring were referenced based on the angle between the line from the position on the ring to the ring center and the initial ingression axis. Linear interpolation in time was used for every embryo to estimate intensity in the intermediate time points to perform averaging. Measured intensities were divided by arc length and averaged between different embryos to obtain mean GFP fluorescence per unit length for different angular ranges and the average for all angles. Total ring GFP fluorescence was calculated by integrating over ring perimeter. Cortical intensities were quantified by choosing the time point with the ring size closest to $\bar{R} = 0.8$ and measuring total fluorescence in the 15th plane after correction for depth attenuation and subtraction of background fluorescence.

Measurements of myosin::GFP fluorescence in the ring at the 4-cell stage were performed as described in Carvalho et. al., 2009. However background fluorescence was determined as the mean fluorescence within a variable size circle at least 10 pixels in diameter, instead of fixed at 10 pixels, to improve measurement quality.

Derivation of the Cortical Flow Feedback (CoFFee) model for cytokinesis

The CoFFee model formalizes the following conceptual view of cytokinesis: Active RhoA recruits contractile ring components to the equatorial cortex, where myosin engages with actin to exert an isotropic force that compresses the underlying cortex. Polar relaxation releases tension in the direction perpendicular to the ring, but not in the around-the-ring direction, generating anisotropic boundary conditions that cause the system to exhibit distinct behavior in the two directions. Disassembly in the around-the-ring direction reduces ring components in proportion to the reduction in length, and does not alter the per unit length amount of myosin. Thus, changes in myosin levels are determined solely by ring-directed cortical flow along the direction perpendicular to the ring, which can be solved as a one-dimensional problem. We assume that the cortical compression rate (between x and $x + dx$) is proportional to local myosin concentration, $m(x,t)$, which exerts stress onto the actin network resulting in

$$\frac{\delta\varepsilon}{\delta t}(x,t) = -\alpha m(x,t), \qquad (18)$$

where ε is the cortical strain (i.e. change in length of cortical surface per unit length) and α is a proportionality constant that reflects the ability of the cortex to be compressed by ring myosin. The velocity of cortical surface movement is obtained from the following relationship (see also equation (12)).

$$v(x,t) = \int_0^x \frac{\delta\varepsilon}{\delta t}(x',t)dx'. \qquad (19)$$

The conservation of mass for myosin flow results in the following

$$\frac{\partial m}{\partial t}(x,t) = -\frac{\partial}{\partial x}\big(m(x,t)v(x,t)\big) = \frac{\partial}{\partial x}\left(m(x,t)\int_0^x \alpha m(x',t)dx'\right). \qquad (20)$$

If we integrate equation (20) over *x* on *(-w, w)* domain we obtain

$$dM_{ring}(t)/dt = \alpha m_{cort} M_{ring}(t), \qquad (21)$$

where $M_{ring}(t) \coloneqq \int_{-w}^{w} m(x,t)dx$ is the total per unit length amount of engaged ring myosin, $2w$ is the width of the contractile ring/active zone where myosin is engaged and compressing cortex and $m_{cort} \coloneqq m(w,t)$ is the concentration of myosin on the cortex delivered into the contractile ring. The velocity of ring-directed cortical flow is

$$v_{flow}(t) = \alpha M_{ring}(t)/2, \qquad (22)$$

The one half is included to account for the fact that flow comes in from both sides. The solution of equation (21) is

$$M_{ring}(t) = M_{0\,ring}\, e^{t/\tau}, \qquad (23)$$

where we define the characteristic time of myosin accumulation, τ, as $\frac{1}{\alpha m_{cort}}$. Note that the total amount of myosin in the ring will be the amount of engaged myosin plus an added baseline that would include any myosin not involved in compression (see equation (5)). We assume the rate of ring shrinkage is proportional to the amount of ring myosin, as observed in our data,

$$\frac{1}{R}\frac{dR}{dt} = -\beta M_{ring}(t), \tag{24}$$

where β is a proportionality coefficient that reflects the ability of the ring to be constricted by ring myosin. Using equations (23) and (24), we obtain the dynamics of contractile ring size over time

$$\bar{R}(t) = \bar{R}_{ini} e^{-\beta\tau M_{0\,ring} \exp(t/\tau)}, \tag{25}$$

where $\bar{R}_{ini}$ is the dimensionless characteristic size of the ring; essentially the radius at minus infinity if the same exponential process controlling contractile ring assembly extended back in time infinitely. Instead, *in vivo* cytokinesis initiates when spindle-based signaling activates RhoA on the equatorial cortex leading to the abrupt recruitment of contractile ring components. If the time frame of reference is chosen so that $t = 0$ is cytokinesis onset immediately following the initial patterning of the cortex by RhoA, $M_{0\,ring}$ is the amount of ring myosin immediately following this event and the initial size of the ring is

$$\bar{R}_0(t) = \bar{R}_{ini} e^{-\beta\tau M_{0\,ring}}. \tag{26}$$

To compare our model with data we use the time frame of reference where $t = 0$ is the point of 50% closure (i.e. $\bar{R}(t = 0) = \frac{1}{2}$). In this reference, $M_{0\,ring} = \frac{\ln(\bar{R}_{ini})}{\beta\tau}$, and by defining dimensionless velocity as $\bar{v} := \tau v$, we obtain equations (4-8). Note that equation (4) can be rewritten in the following way

$$\bar{R}(\bar{t}) = \bar{R}_{ini} e^{-\frac{1}{\bar{R}}\frac{d\bar{R}}{d\bar{t}}}, \tag{27}$$

where $\bar{t} \coloneqq t/\tau$. This relationship implies that in this dimensionless time, where $\bar{R}(\bar{t} = 0) = \frac{1}{2}$, any two rings of the same size have the same dimensionless constriction rate.

Data availability

All data is available from the authors upon request.

Code availability

The custom computer code used in this study is freely available from the authors upon request.

ACKNOWLEDGEMENTS

This work was supported by a fellowship from the Jane Coffin Childs Memorial Fund to R.N.K. and grants to M.W.B from AFOSR (FA9550-08-1-0284) and the Beckman Laser Institute Foundation. J.S.G-C was supported by the University of California, San Diego Cancer Cell Biology Training Program (T32 CA067754). A.D. and K.O. receive salary and other support from the Ludwig Institute for Cancer Research.

REFERENCES

Biron, D., Libros, P., Sagi, D., Mirelman, D., & Moses, E. (2004). Biphasic cytokinesis and cooperative single cell re-production. In A. T. Skejeltorp & A. V. Belushkin (Eds.), *Forces, Growth and Form in Soft Condensed Matter: At the Interface between Physics and Biology* (pp. 217-234): Springer, Berlin.

Bluemink, J. G., & de Laat, S. W. (1973). New membrane formation during cytokinesis in normal and cytochalasin B-treated eggs of Xenopus laevis. I. Electron microscope observations. *J Cell Biol, 59*(1), 89-108.

Botvinick, E. L., & Berns, M. W. (2005). Internet-based robotic laser scissors and tweezers microscopy. *Microsc Res Tech, 68*(2), 65-74. doi:10.1002/jemt.20216

Bourdages, K. G., Lacroix, B., Dorn, J. F., Descovich, C. P., & Maddox, A. S. (2014). Quantitative analysis of cytokinesis in situ during C. elegans postembryonic development. *PLoS One, 9*(10), e110689. doi:10.1371/journal.pone.0110689

Byers, T. J., & Armstrong, P. B. (1986). Membrane protein redistribution during Xenopus first cleavage. *J Cell Biol, 102*(6), 2176-2184.

Calvert, M. E., Wright, G. D., Leong, F. Y., Chiam, K. H., Chen, Y., Jedd, G., & Balasubramanian, M. K. (2011). Myosin concentration underlies cell size-dependent scalability of actomyosin ring constriction. *J Cell Biol, 195*(5), 799-813. doi:10.1083/jcb.201101055

Canman, J. C., Hoffman, D. B., & Salmon, E. D. (2000). The role of pre- and post-anaphase microtubules in the cytokinesis phase of the cell cycle. *Curr Biol, 10*(10), 611-614.

Cao, L. G., & Wang, Y. L. (1990). Mechanism of the formation of contractile ring in dividing cultured animal cells. II. Cortical movement of microinjected actin filaments. *J Cell Biol, 111*(5 Pt 1), 1905-1911.

Carvalho, A., Desai, A., & Oegema, K. (2009). Structural memory in the contractile ring makes the duration of cytokinesis independent of cell size. *Cell, 137*(5), 926-937. doi:10.1016/j.cell.2009.03.021

Carvalho, A., Olson, S. K., Gutierrez, E., Zhang, K., Noble, L. B., Zanin, E., . . . Oegema, K. (2011). Acute drug treatment in the early C. elegans embryo. *PLoS One, 6*(9), e24656. doi:10.1371/journal.pone.0024656

Chaudhuri, O., Parekh, S. H., & Fletcher, D. A. (2007). Reversible stress softening of actin networks. *Nature, 445*(7125), 295-298. doi:10.1038/nature05459

Dan, K. (1954). The cortical movement in Arbacia Punctulata eggs through cleavage cycles. *Embryologia, 2*(12), 115-122.

Dan, K., & Dan, J. C. (1940). Behavior of the Cell Surface during Cleavage: III. On the formation of New Surface in the Eggs of Strongylocentrotus Pulcherrimus. *Biological Bulletin, 78*(3), 486-501.

Dan, K., Dan, J. C., & Yanagita, T. (1938). Behaviour of the Cell Surface During Cleavage. II. *Cytologia, 8*, 521-531.

Dan, K., & Ono, T. (1954). A method of computation of the surface area of the cell. *Embryologia, 2*, 87-98.

Dan, K., Yanagita, T., & Sugiyama, M. (1937). Behavior of the cell surface during cleavage. I. *Protoplasma, 28*, 68-81.

Danilchik, M. V., Bedrick, S. D., Brown, E. E., & Ray, K. (2003). Furrow microtubules and localized exocytosis in cleaving Xenopus laevis embryos. *J Cell Sci, 116*(Pt 2), 273-283.

Davies, T., Jordan, S. N., Chand, V., Sees, J. A., Laband, K., Carvalho, A. X., . . . Canman, J. C. (2014). High-resolution temporal analysis reveals a functional timeline for the molecular regulation of cytokinesis. *Dev Cell, 30*(2), 209-223. doi:10.1016/j.devcel.2014.05.009

DeBiasio, R. L., LaRocca, G. M., Post, P. L., & Taylor, D. L. (1996). Myosin II transport, organization, and phosphorylation: evidence for cortical flow/solation-contraction coupling during cytokinesis and cell locomotion. *Mol Biol Cell, 7*(8), 1259-1282.

Dickinson, D. J., Ward, J. D., Reiner, D. J., & Goldstein, B. (2013). Engineering the Caenorhabditis elegans genome using Cas9-triggered homologous recombination. *Nat Methods, 10*(10), 1028-1034. doi:10.1038/nmeth.2641

Edelstein, A. D., Tsuchida, M. A., Amodaj, N., Pinkard, H., Vale, R. D., & Stuurman, N. (2014). Advanced methods of microscope control using muManager software. *J Biol Methods, 1*(2). doi:10.14440/jbm.2014.36

Essex, A., Dammermann, A., Lewellyn, L., Oegema, K., & Desai, A. (2009). Systematic analysis in Caenorhabditis elegans reveals that the spindle checkpoint is composed of two largely independent branches. *Mol Biol Cell, 20*(4), 1252-1267. doi:10.1091/mbc.E08-10-1047

Farnebäck, G. (2003). Two-frame motion estimation based on polynomial expansion lecture notes in computer science (pp. 363-370): Springer Science and Buisness Media.

Fededa, J. P., & Gerlich, D. W. (2012). Molecular control of animal cell cytokinesis. *Nat Cell Biol, 14*(5), 440-447. doi:10.1038/ncb2482

Fishkind, D. J., Silverman, J. D., & Wang, Y. L. (1996). Function of spindle microtubules in directing cortical movement and actin filament organization in dividing cultured cells. *J Cell Sci, 109 (Pt 8)*, 2041-2051.

Frokjaer-Jensen, C., Davis, M. W., Hopkins, C. E., Newman, B. J., Thummel, J. M., Olesen, S. P., . . . Jorgensen, E. M. (2008). Single-copy insertion of transgenes in Caenorhabditis elegans. *Nat Genet, 40*(11), 1375-1383. doi:10.1038/ng.248

Gardel, M. L., Schneider, I. C., Aratyn-Schaus, Y., & Waterman, C. M. (2010). Mechanical integration of actin and adhesion dynamics in cell migration. *Annu Rev Cell Dev Biol, 26*, 315-333. doi:10.1146/annurev.cellbio.011209.122036

Green, R. A., Paluch, E., & Oegema, K. (2012). Cytokinesis in animal cells. *Annu Rev Cell Dev Biol, 28*, 29-58. doi:10.1146/annurev-cellbio-101011-155718

Greenspan, H. P. (1978). On fluid-mechanical simulations of cell division and movement. *J Theor Biol, 70*, 125-134.

Gudejko, H. F., Alford, L. M., & Burgess, D. R. (2012). Polar expansion during cytokinesis. *Cytoskeleton (Hoboken), 69*(11), 1000-1009. doi:10.1002/cm.21078

Hickson, G. R., Echard, A., & O'Farrell, P. H. (2006). Rho-kinase controls cell shape changes during cytokinesis. *Curr Biol, 16*(4), 359-370. doi:10.1016/j.cub.2005.12.043

Hird, S. N., & White, J. G. (1993). Cortical and cytoplasmic flow polarity in early embryonic cells of Caenorhabditis elegans. *J Cell Biol, 121*(6), 1343-1355.

Jordan, S. N., & Canman, J. C. (2012). Rho GTPases in animal cell cytokinesis: an occupation by the one percent. *Cytoskeleton (Hoboken), 69*(11), 919-930. doi:10.1002/cm.21071

Ma, X., Kovacs, M., Conti, M. A., Wang, A., Zhang, Y., Sellers, J. R., & Adelstein, R. S. (2012). Nonmuscle myosin II exerts tension but does not translocate actin in vertebrate cytokinesis. *Proc Natl Acad Sci U S A, 109*(12), 4509-4514. doi:10.1073/pnas.1116268109

Mabuchi, I. (1994). Cleavage furrow: timing of emergence of contractile ring actin filaments and establishment of the contractile ring by filament bundling in sea urchin eggs. *J Cell Sci, 107 (Pt 7)*, 1853-1862.

Maddox, A. S., Lewellyn, L., Desai, A., & Oegema, K. (2007). Anillin and the septins promote asymmetric ingression of the cytokinetic furrow. *Dev Cell, 12*(5), 827-835. doi:10.1016/j.devcel.2007.02.018

Mandato, C. A., & Bement, W. M. (2003). Actomyosin transports microtubules and microtubules control actomyosin recruitment during Xenopus oocyte wound healing. *Curr Biol, 13*(13), 1096-1105.

Martineau, S. N., Andreassen, P. R., & Margolis, R. L. (1995). Delay of HeLa cell cleavage into interphase using dihydrocytochalasin B: retention of a postmitotic spindle and telophase disc correlates with synchronous cleavage recovery. *J Cell Biol, 131*(1), 191-205.

Matsumura, F. (2005). Regulation of myosin II during cytokinesis in higher eukaryotes. *Trends Cell Biol, 15*(7), 371-377. doi:10.1016/j.tcb.2005.05.004

Mayer, M., Depken, M., Bois, J. S., Julicher, F., & Grill, S. W. (2010). Anisotropies in cortical tension reveal the physical basis of polarizing cortical flows. *Nature, 467*(7315), 617-621. doi:10.1038/nature09376

Munjal, A., & Lecuit, T. (2014). Actomyosin networks and tissue morphogenesis. *Development, 141*(9), 1789-1793. doi:10.1242/dev.091645

Murrell, M., Oakes, P. W., Lenz, M., & Gardel, M. L. (2015). Forcing cells into shape: the mechanics of actomyosin contractility. *Nat Rev Mol Cell Biol, 16*(8), 486-498. doi:10.1038/nrm4012

Naganathan, S. R., Furthauer, S., Nishikawa, M., Julicher, F., & Grill, S. W. (2014). Active torque generation by the actomyosin cell cortex drives left-right symmetry breaking. *Elife, 3*, e04165. doi:10.7554/eLife.04165

Pelham, R. J., & Chang, F. (2002). Actin dynamics in the contractile ring during cytokinesis in fission yeast. *Nature, 419*(6902), 82-86. doi:10.1038/nature00999

Piekny, A., Werner, M., & Glotzer, M. (2005). Cytokinesis: welcome to the Rho zone. *Trends Cell Biol, 15*(12), 651-658. doi:10.1016/j.tcb.2005.10.006

Piekny, A. J., & Mains, P. E. (2002). Rho-binding kinase (LET-502) and myosin phosphatase (MEL-11) regulate cytokinesis in the early Caenorhabditis elegans embryo. *J Cell Sci, 115*(Pt 11), 2271-2282.

Reymann, A. C., Staniscia, F., Erzberger, A., Salbreux, G., & Grill, S. W. (2016). Cortical flow aligns actin filaments to form a furrow. *Elife, 5*. doi:10.7554/eLife.17807

Rodrigues, N. T., Lekomtsev, S., Jananji, S., Kriston-Vizi, J., Hickson, G. R., & Baum, B. (2015). Kinetochore-localized PP1-Sds22 couples chromosome segregation to polar relaxation. *Nature, 524*(7566), 489-492. doi:10.1038/nature14496

Salbreux, G., Charras, G., & Paluch, E. (2012). Actin cortex mechanics and cellular morphogenesis. *Trends Cell Biol, 22*(10), 536-545. doi:10.1016/j.tcb.2012.07.001

Schonegg, S., Hyman, A. A., & Wood, W. B. (2014). Timing and mechanism of the initial cue establishing handed left-right asymmetry in Caenorhabditis elegans embryos. *Genesis, 52*(6), 572-580.

Schroeder, T. E. (1975). Dynamics of the contractile ring. *Soc Gen Physiol Ser, 30*, 305-334.

Schroeder, T. E. (1990). The contractile ring and furrowing in dividing cells. *Ann N Y Acad Sci, 582*, 78-87.

Sedzinski, J., Biro, M., Oswald, A., Tinevez, J. Y., Salbreux, G., & Paluch, E. (2011). Polar actomyosin contractility destabilizes the position of the cytokinetic furrow. *Nature, 476*(7361), 462-466. doi:10.1038/nature10286

Seidel, H. S., Ailion, M., Li, J., van Oudenaarden, A., Rockman, M. V., & Kruglyak, L. (2011). A novel sperm-delivered toxin causes late-stage embryo lethality and transmission ratio distortion in C. elegans. *PLoS Biol, 9*(7), e1001115. doi:10.1371/journal.pbio.1001115

Selman, G. G., & Perry, M. M. (1970). Ultrastructural changes in the surface layers of the newt's egg in relation to the mechanism of its cleavage. *J Cell Sci, 6*(1), 207-227.

Straight, A. F., Cheung, A., Limouze, J., Chen, I., Westwood, N. J., Sellers, J. R., & Mitchison, T. J. (2003). Dissecting temporal and spatial control of cytokinesis with a myosin II Inhibitor. *Science, 299*(5613), 1743-1747. doi:10.1126/science.1081412

Swann, M. M., & Mitchison, J. M. (1958). Cleavage in animal cells. *Biological Reviews, 33*(1), 103-135.

Taber, L. A. (1995). Biomechanics of growth, remodeling, and morphogenesis. *Appl Mech Rev, 48*(8), 487-545.

Tseng, Y., & Wirtz, D. (2004). Dendritic branching and homogenization of actin networks mediated by arp2/3 complex. *Phys Rev Lett, 93*(25), 258104. doi:10.1103/PhysRevLett.93.258104

Turlier, H., Audoly, B., Prost, J., & Joanny, J. F. (2014). Furrow constriction in animal cell cytokinesis. *Biophys J, 106*(1), 114-123. doi:10.1016/j.bpj.2013.11.014

Vale, R. D., Spudich, J. A., & Griffis, E. R. (2009). Dynamics of myosin, microtubules, and Kinesin-6 at the cortex during cytokinesis in Drosophila S2 cells. *J Cell Biol, 186*(5), 727-738. doi:10.1083/jcb.200902083

Wang, Y. L., Silverman, J. D., & Cao, L. G. (1994). Single particle tracking of surface receptor movement during cell division. *J Cell Biol, 127*(4), 963-971.

White, J. G., & Borisy, G. G. (1983). On the mechanisms of cytokinesis in animal cells. *J Theor Biol, 101*(2), 289-316.

Wolpert, L. (1960). The mechanics and mechanism of cleavage. *International review of cytology, 10*, 163-216.

Wu, J. Q., & Pollard, T. D. (2005). Counting cytokinesis proteins globally and locally in fission yeast. *Science, 310*(5746), 310-314. doi:10.1126/science.1113230

Xiong, H., Mohler, W. A., & Soto, M. C. (2011). The branched actin nucleator Arp2/3 promotes nuclear migrations and cell polarity in the C. elegans zygote. *Dev Biol, 357*(2), 356-369. doi:10.1016/j.ydbio.2011.07.008

Yumura, S. (2001). Myosin II dynamics and cortical flow during contractile ring formation in Dictyostelium cells. *J Cell Biol, 154*(1), 137-146.

Zhou, M., & Wang, Y. L. (2008). Distinct pathways for the early recruitment of myosin II and actin to the cytokinetic furrow. *Mol Biol Cell, 19*(1), 318-326. doi:10.1091/mbc.E07-08-0783

Zhu, Z., Chai, Y., Jiang, Y., Li, W., Hu, H., Li, W., . . . Ou, G. (2016). Functional Coordination of WAVE and WASP in C. elegans Neuroblast Migration. *Dev Cell, 39*(2), 224-238. doi:10.1016/j.devcel.2016.09.029

Zinemanas, D., & Nir, A. (1987). Fluid mechanical simulations of cell furrowing due to anisotropic surface forces. In N. Akkas (Ed.), *Biomechanics of cell division* (pp. 281-305): Plenum Press, New York.

Zinemanas, D., & Nir, A. (1988). On the viscous deformation of biological cells under anisotropic surface tension. *J Fluid Mech, 193*, 217-241.

Zumdieck, A., Kruse, K., Bringmann, H., Hyman, A. A., & Julicher, F. (2007). Stress generation and filament turnover during actin ring constriction. *PLoS One, 2*(8), e696. doi:10.1371/journal.pone.0000696

FIGURES AND FIGURE LEGENDS

Figure 1

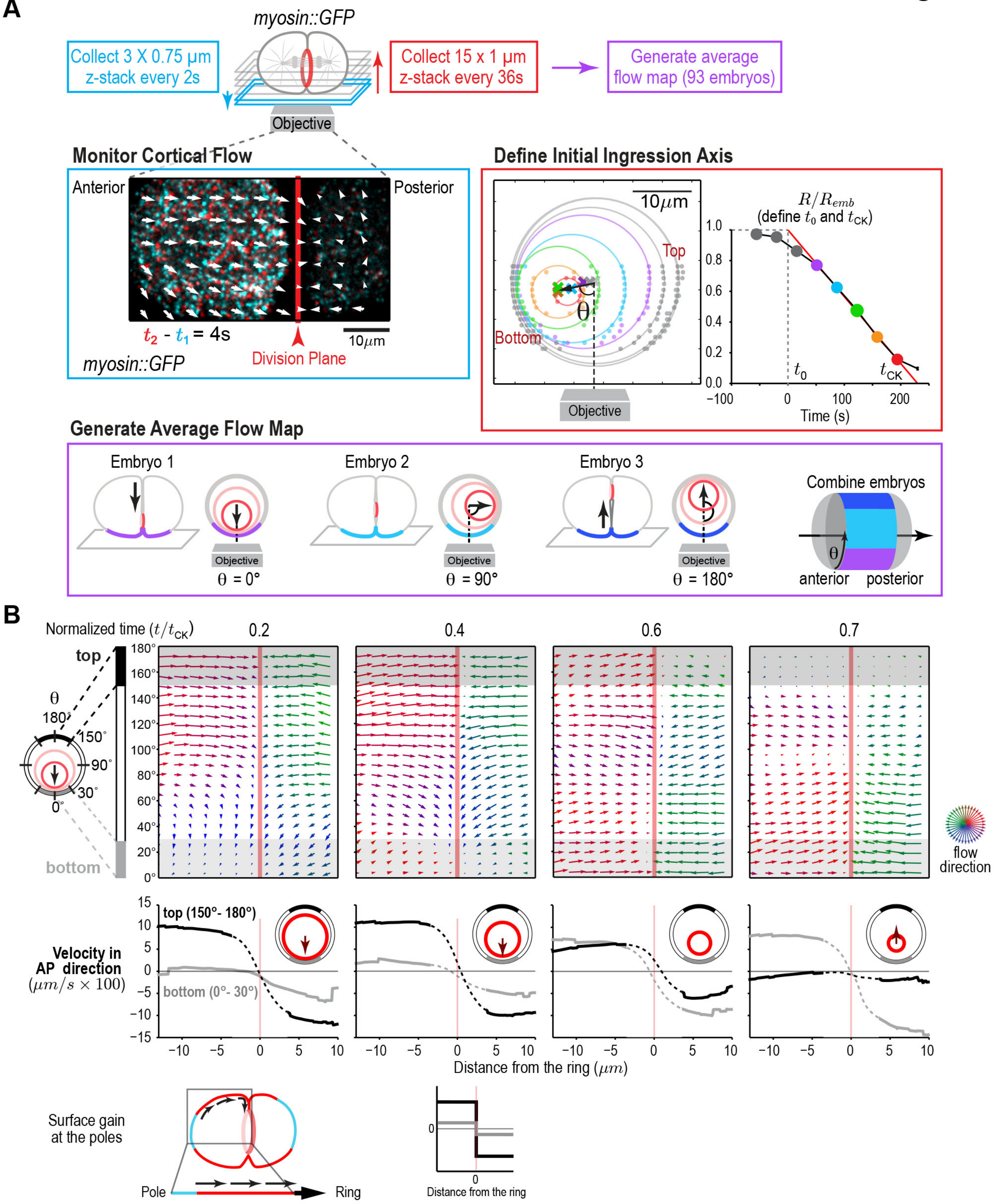

Figure 1. **An average cortical flow map reveals that surface gain occurs at the cell poles.** (**A**) (*top*) Schematic of the experimental procedure. (*middle, left*) Superposition of images of the cortex acquired 4s apart. Arrows indicate cortical flow (magnified 2.5X). (*middle, right*) The initial ingression axis, t_0, and t_{CK} were defined as shown for a representative embryo. The angle θ specifies the position of the imaged cortex relative to the initial ingression axis. Image and quantification are representative of the 93 imaged embryos. (*bottom*) Angular position was used to combine data from 93 embryos to generate an average flow map. (**B**) (*top*) Average flow at the indicated timepoints. Arrows show direction and magnitude of the displacement in 2s (magnified 20X). (*middle*) Graphs are average velocity in the A-P direction versus position along the A-P axis for the cortex on the top (*black*) and bottom (*grey*) of the embryo (*shaded in flow maps*). Surface movement changes direction across the division plane, the apparent velocity gradient close to the division plane is a projection artifact due to surface curvature (dotted regions on velocity curves). (*bottom*) Schematics show a one-dimensional representation and expected cortical velocity plot for surface gain at the poles.

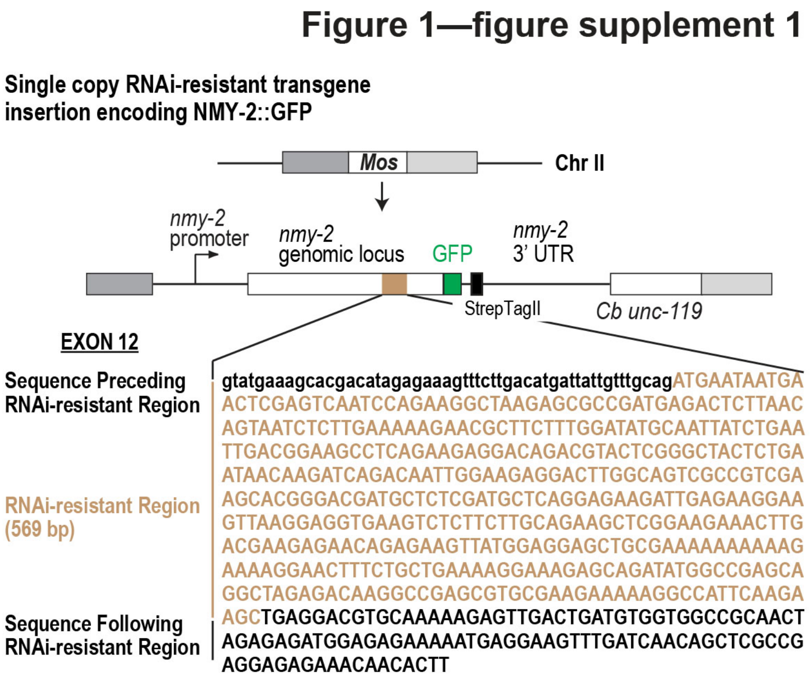

Figure 1 – Figure Supplement 1. Schematic of the single-copy *nmy-2::gfp* transgene inserted into a specific locus on chromosome II. Cb *unc-119*, the *unc-119* coding region from the related nematode *C. briggsae*, was used as a transformation marker. The transgene was re-encoded while maintaining amino acid sequence in the indicated region to render it resistant to RNAi targeting the endogenous gene for other experiments, we did not use this feature in the experiments reported here.

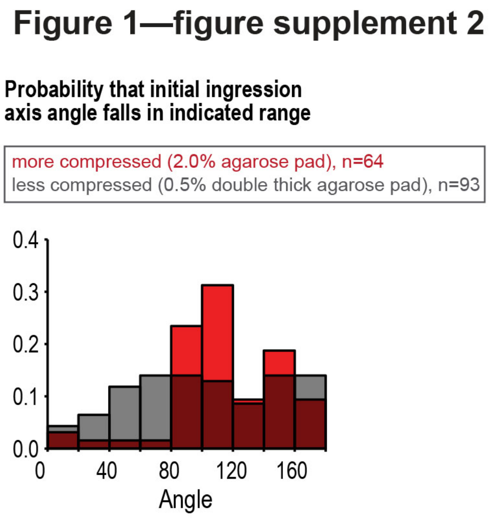

Figure 1 – Figure Supplement 2. Compression biases the direction of contractile ring closure. Graph plotting the probability that the angle between the objective axis and the initial ingression axis falls in the indicated range for embryos mounted with more *(red*) or less (*grey*) compression.

Figure 1—figure supplement 3

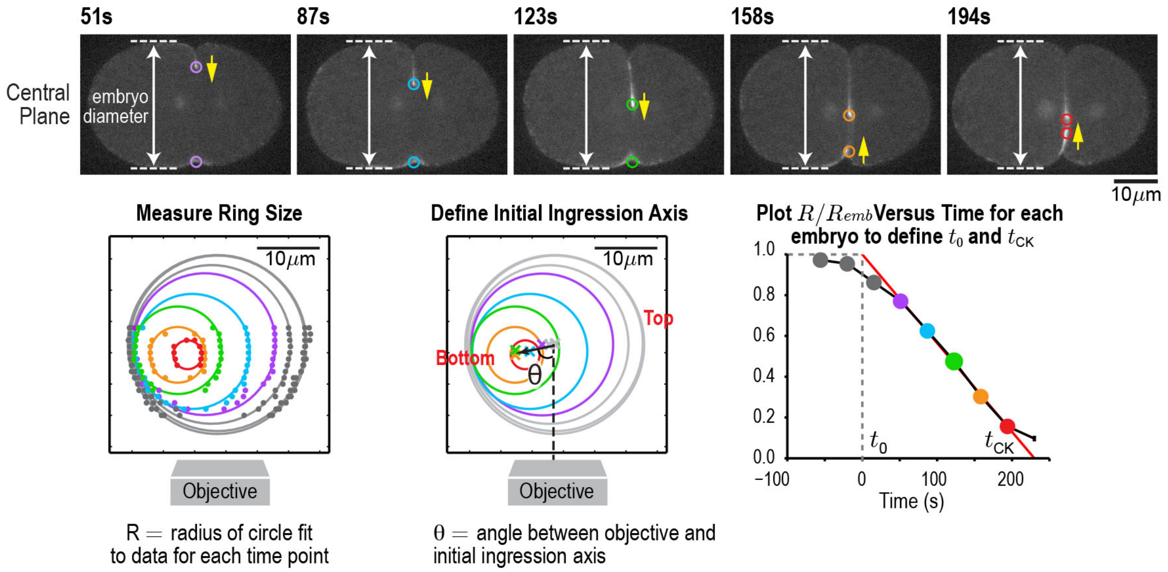

Figure 1 – Figure Supplement 3. An automated method for monitoring contractile ring closure. (*top*) Central plane images of the embryo in Figure 1A. Panels on the lower left and lower right are reproduced from Figure 1A for comparison. An automated algorithm was used to identify the edges of the embryo (dashed lines) and the position of the contractile ring (colored circles) in each z-plane. Yellow arrows mark the direction of furrow ingression and illustrate how the furrow initially ingresses from the top and then changes directions to ingress from the bottom during the second half of cytokinesis. (*lower left*) Points marking contractile ring position in the z-planes were projected onto an end-on view of the division plane. Data for different timepoints in this representative embryo are shown in colors corresponding to the circles in the central plane images. Ring sizes were measured by fitting circles to the data. (*middle*) The initial axis of contractile ring closure was defined by the angle θ between the objective axis and a line fit through the centers of the contractile rings with a normalized size > 0.3. (*right*) = A plot of normalized ring size versus time for this embryo defines t_0 and t_{CK} as the times when a line fit through the points corresponding to ring sizes between 0.3 and 0.8 crossed 1 and 0, respectively. Scale bar is 10μm.

Figure 1—figure supplement 4

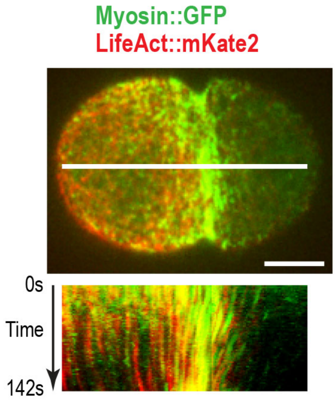

Figure 1 – Figure Supplement 4. Actin and myosin move together with the cortical surface during cytokinesis. The white line in the center of the image (*top*) indicates the region used for the kymograph (*bottom*). Image is representative of 5 imaged embryos. Scale bar is 10μm.

Figure 1—figure supplement 5

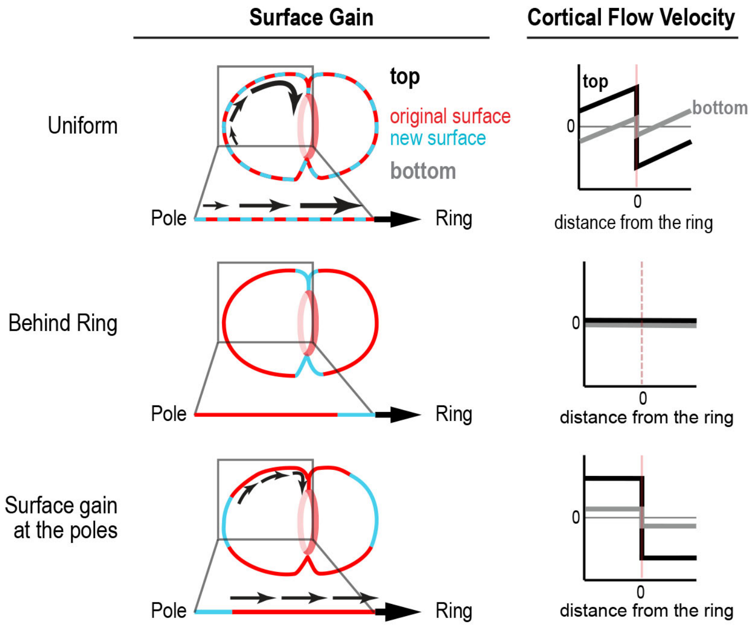

Figure 1 – Figure Supplement 5. Different profiles of cortical surface velocity along the A-P axis are predicted for different spatial patterns of surface gain. (*top*) For surface gain behind the ring, no cortical movement is predicted on the embryo surface. (*middle*) For uniform surface gain, a gradient of velocities will be observed, where the cortex immediately behind the ring moves at the speed of the ingressing furrow, and cortical velocity decreases linearly towards the cell poles. (*bottom*) Reproduced from Figure 1B for comparison. If surface is gained only at the poles, cortical velocity will be constant in magnitude within the flow map region with opposite direction on the two sides of the embryo.

Figure 2

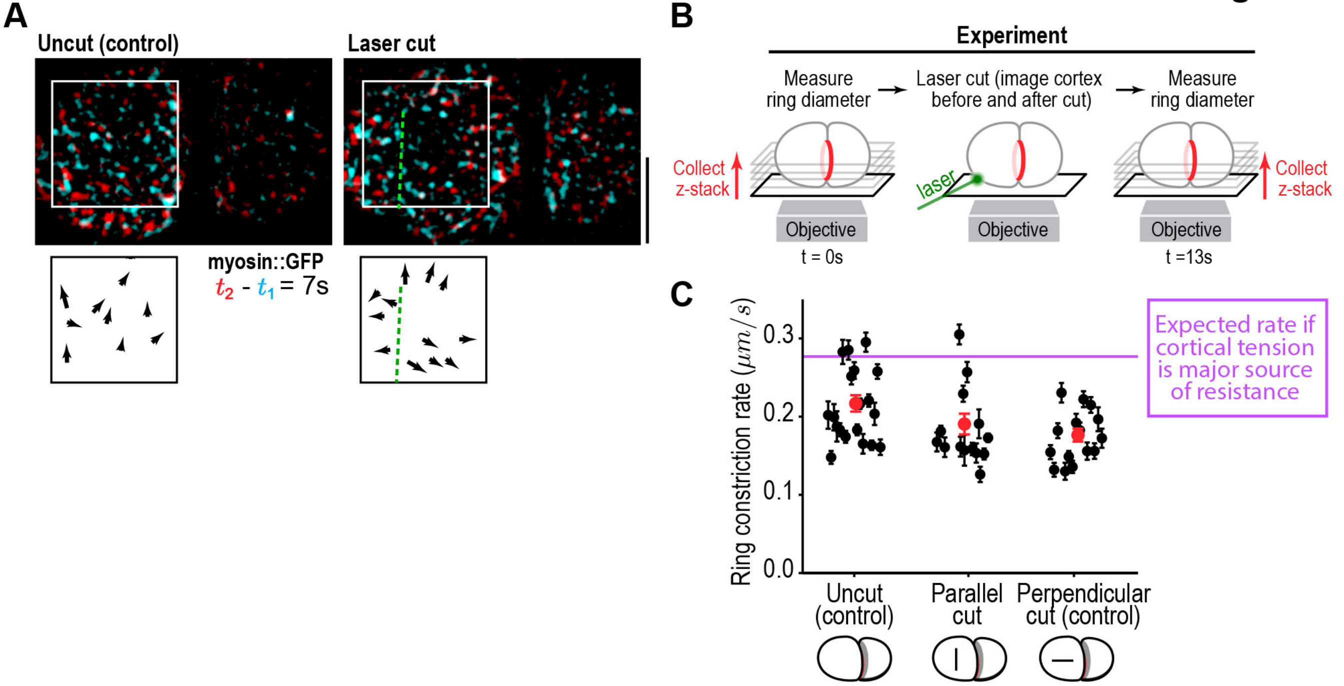

Figure 2. Cortical tension does not limit the rate of ring closure. (**A**) The success of cortical cuts was assessed by comparing surface images of cortical myosin before (*cyan*) and after (*red*) the cut to monitor the movement of myosin foci away from the cut site. Representative images from 1 out of 48 embryos imaged are shown. Scale bar is 10 µm. (**B**) Schematic of laser ablation experiment to determine if cortical resistance limits the rate of contractile ring closure. Contractile ring sizes were measured from z-stacks acquired before and after a cut was made across the cortex with a laser. (**C**) Graph plots the rates of ring closure derived from before and after ring size measurements for uncut controls (n=19 embryos) and embryos with cuts perpendicular (n=15 embryos) or parallel (n=14 embryos) to the ring. Black symbols are single embryo measurements with measurement errors. Red symbols are the means; error bars are the SEM. The purple line marks expected closure rate if cortical tension is a major source of resistance.

Figure 2—figure supplement 1

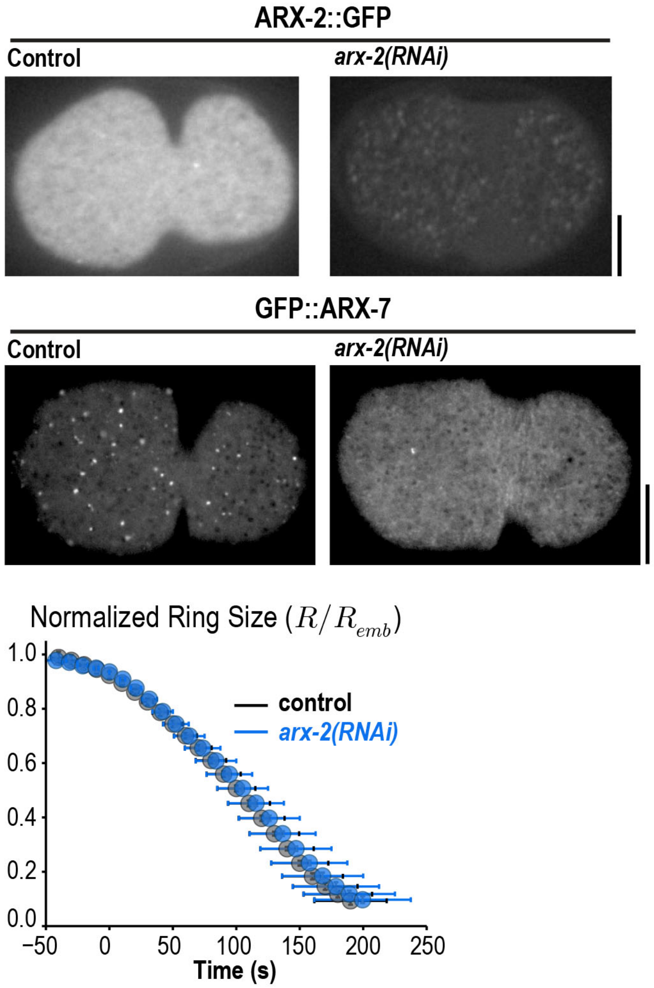

Figure 2 – Figure Supplement 1. Arp2/3 depletion does not alter ring constriction kinetics. Images of cortical ARX-2::GFP and GFP::ARX-7 in control and *arx-2(RNAi)* embryos confirm loss of cortical Arp2/3 complex (images are representative of 10 imaged embryos for each condition in the GFP::ARX-7 strain and 15 for control and 13 for *arx-2(RNAi)* in the ARX-2::GFP strain). Scale bars are 10μm. Graph plots average contractile ring size versus time for control (grey) and *arx-2(RNAi)* (blue) embryos expressing myosin::GFP (n= 93 embryos for control and 68 embryos for *arx-2(RNAi)*). Error bars are standard deviation.

Figure 2—figure supplement 2

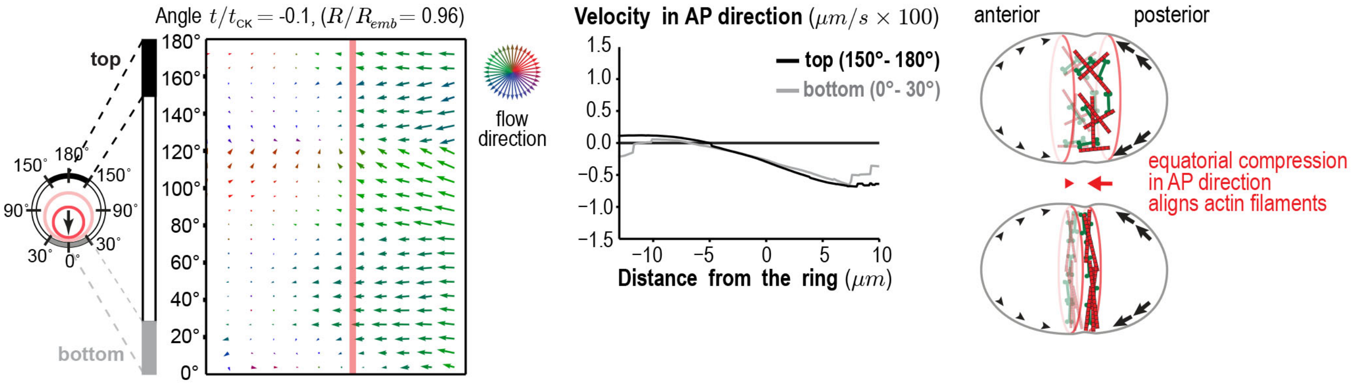

Figure 2 – Figure Supplement 2. An equatorial zone of cortical compression is observed during contractile ring assembly. (*left*) Average flow map at (t/t_{CK}=-0.1) immediately after spindle-based signaling has recruited myosin and other contractile ring components to the equatorial cortex (n= 93 embryos). (*middle*) The surface velocity profile reveals a velocity gradient that spans the cell equator (-5 to +5 µm), indicating a zone of cortical compression. (*right*) Schematic depicting how polar expansion in response to tension generated by the forming ring contributes to equatorial filament alignment during ring assembly.

Figure 3

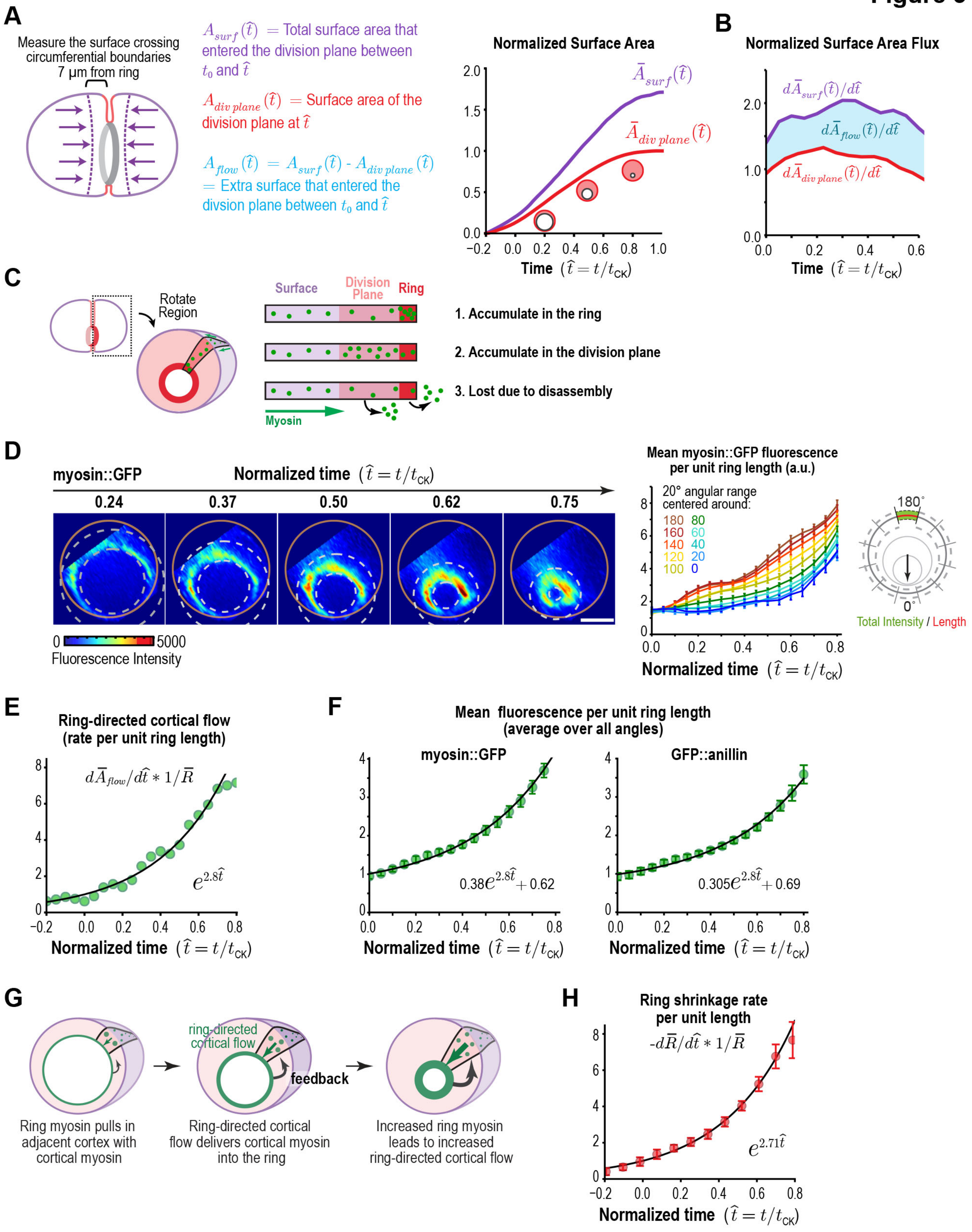
A
Measure the surface crossing circumferential boundaries 7 µm from ring
$A_{surf}(\hat{t})$ = Total surface area that entered the division plane between t_0 and $\hat{t}$
$A_{div\ plane}(\hat{t})$ = Surface area of the division plane at $\hat{t}$
$A_{flow}(\hat{t}) = A_{surf}(\hat{t}) - A_{div\ plane}(\hat{t})$ = Extra surface that entered the divsion plane between t_0 and $\hat{t}$
Normalized Surface Area
$\bar{A}_{surf}(\hat{t})$
$\bar{A}_{div\ plane}(\hat{t})$
2.0
1.5
1.0
0.5
0.0
−0.2
0.0
0.2
0.4
0.6
0.8
1.0
Time $(\hat{t} = t/t_{CK})$
B
Normalized Surface Area Flux
$d\bar{A}_{surf}(\hat{t})/d\hat{t}$
$d\bar{A}_{flow}(\hat{t})/d\hat{t}$
$d\bar{A}_{div\ plane}(\hat{t})/d\hat{t}$
2.0
1.0
0.0
0.0
0.2
0.4
0.6
Time $(\hat{t} = t/t_{CK})$
C
Rotate Region
Surface
Division Plane
Ring
1. Accumulate in the ring
2. Accumulate in the division plane
3. Lost due to disassembly
Myosin
D
myosin::GFP
Normalized time $(\hat{t} = t/t_{CK})$
0.24
0.37
0.50
0.62
0.75
0
5000
Fluorescence Intensity
Mean myosin::GFP fluorescence per unit ring length (a.u.)
20° angular range centered around:
180 80
160 60
140 40
120 20
100 0
8
6
4
2
0
0.0
0.2
0.4
0.6
0.8
Normalized time $(\hat{t} = t/t_{CK})$
180°
0°
Total Intensity / Length
E
Ring-directed cortical flow (rate per unit ring length)
$d\bar{A}_{flow}/d\hat{t} * 1/\bar{R}$
$e^{2.8\hat{t}}$
8
6
4
2
0
−0.2
0.0
0.2
0.4
0.6
0.8
Normalized time $(\hat{t} = t/t_{CK})$
F
Mean fluorescence per unit ring length (average over all angles)
myosin::GFP
$0.38e^{2.8\hat{t}} + 0.62$
GFP::anillin
$0.305e^{2.8\hat{t}} + 0.69$
4
3
2
1
0
0.0
0.2
0.4
0.6
0.8
Normalized time $(\hat{t} = t/t_{CK})$
G
ring-directed cortical flow
feedback
Ring myosin pulls in adjacent cortex with cortical myosin
Ring-directed cortical flow delivers cortical myosin into the ring
Increased ring myosin leads to increased ring-directed cortical flow
H
Ring shrinkage rate per unit length
$-d\bar{R}/d\hat{t} * 1/\bar{R}$
$e^{2.71\hat{t}}$
8
6
4
2
0
−0.2
0.0
0.2
0.4
0.6
0.8
Normalized time $(\hat{t} = t/t_{CK})$

Figure 3. Cortical surface is compressed into the contractile ring during constriction leading to an exponential increase in the amount of ring components and in the rates of cortical flow and ring constriction. (**A**) Plot comparing the area of the forming division plane (*red*) with the total cortical surface area that entered the division plane from the start of cytokinesis (*purple*; calculated as indicated in the schematic). (**B**) Plot comparing the rate of cortical flow into the division plane (*purple*) with the rate of division plane growth (*red*). (**C**) Possible fates for extra cortical surface delivered to the division plane. (**D**) (*left*) Images of the division plane reconstructed from 40-plane z-stacks. Gold circles mark the embryo boundary and dashed circles mark the boundaries used for ring intensity measurements. (*right*) Graph plots per unit length myosin::GFP fluorescence for the indicated angular ranges (n=36 embryos). Image series is representative of 36 imaged embryos. (**E,F**) Graphs plot per unit length rate of ring-directed cortical flow (n=93 embryos) and mean per unit length myosin::GFP (n=36 embryos) or GFP::anillin (n=26 embryos) fluorescence (n=36 embryos) in the ring. (**G**) Schematic illustrating the proposed feedback loop that drives the parallel exponential increases in ring myosin and in the rates of cortical flow and constriction. (**H**) Graph plots the per unit length rate of ring closure. Black lines are fitted single exponentials. Error bars are the SEM.

Figure 3—figure supplement 1

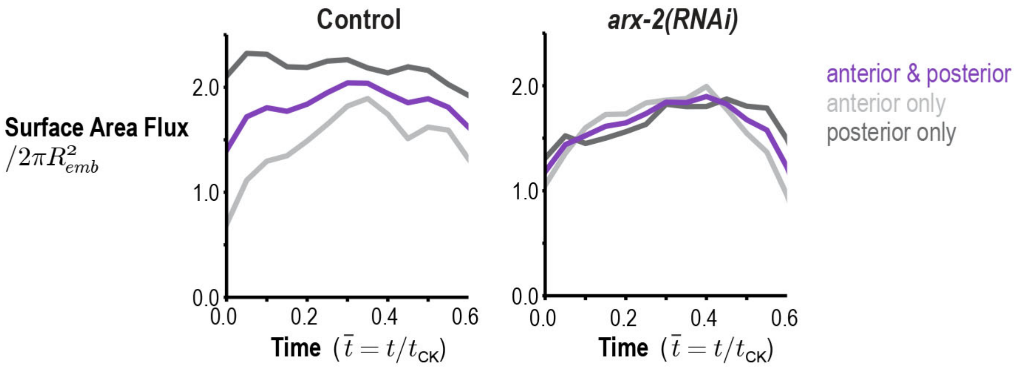

Figure 3 – Figure Supplement 1. Arp2/3 inhibition abolishes the asymmetry in the amount of cortex entering the division plane from the anterior and posterior sides. Graphs plot the rate of cortical flux across the anterior (*light grey*) and posterior (*dark grey*) boundaries (see schematic in Figure 3A) versus the mean for the two sides (*purple*) for control and *arx-2(RNAi)* embryos. Calculated from the average flow maps for the control (n= 93 embryos) and *arx-2(RNAi)* (n= 68 embryos) conditions.

Figure 3—figure supplement 2

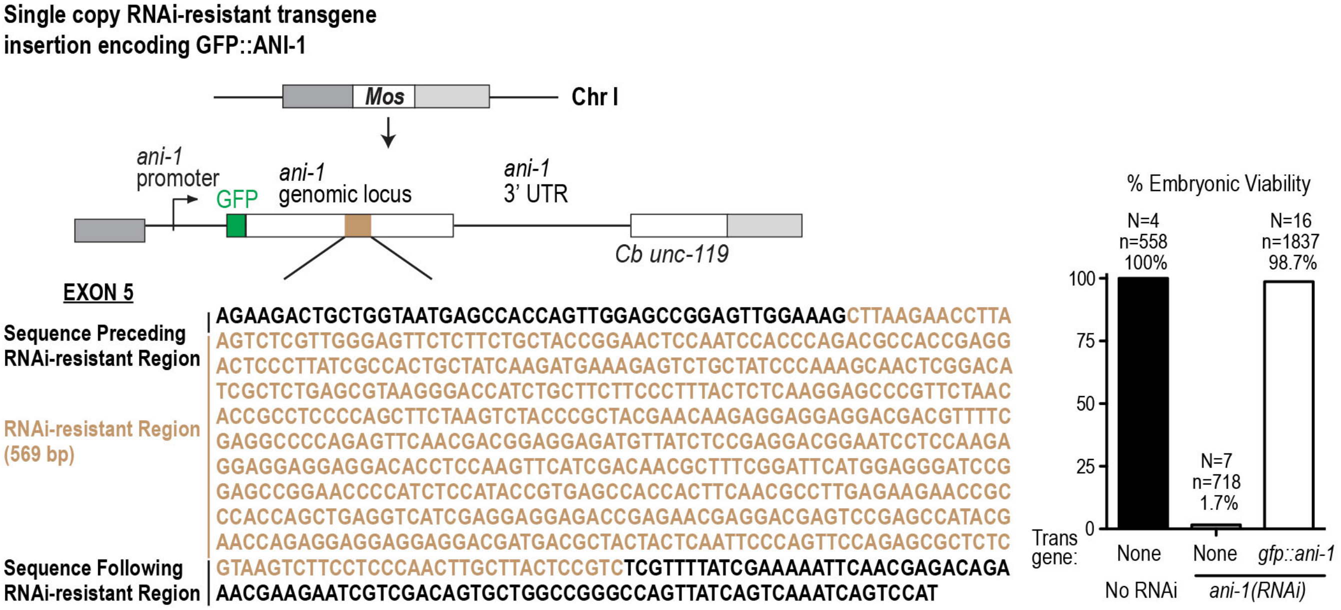

Figure 3 – Figure Supplement 2. The GFP::anillin fusion is functional. (*left*) Schematic of the single-copy *gfp::ani-1* trangene. The transgene was re-encoded while maintaining amino acid sequence in the indicated region to render it resistant to RNAi targeting of the endogenous *ani-1* gene to allow testing of the functionality of the GFP::ANI-1 fusion. (*right*) Graph plotting embryonic lethality demonstrates functionality of the *gfp::ani-1* transgene.

Figure 3—figure supplement 3

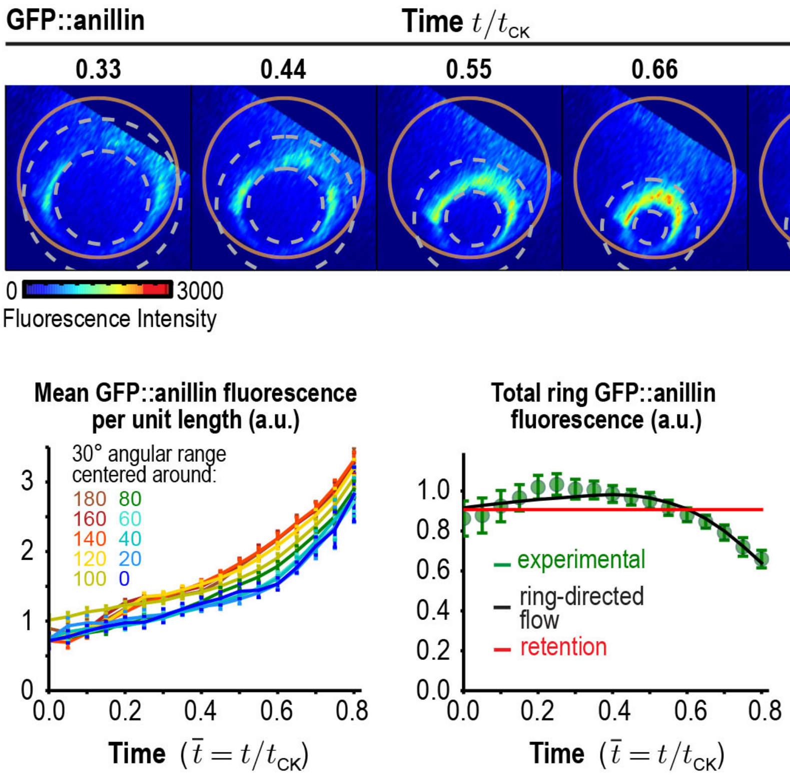

Figure 3 – Figure Supplement 3. GFP::anillin fluorescence in the ring increases exponentially during constriction. (*top*) Images of the division plane in an embryo expressing GFP::anillin. (*bottom, left*) Graph plots GFP::anillin fluorescence per unit length of the ring for the indicated angular ranges. (bottom, *right*) Graph plotting mean total ring fluorescence (average for all angles; *green*) for GFP::anillin (n=26 embryos). The predictions for ring-directed cortical flow (*black*) and the retention (*red*) model are also shown. Error bars are the SEM.

Figure 3—figure supplement 4

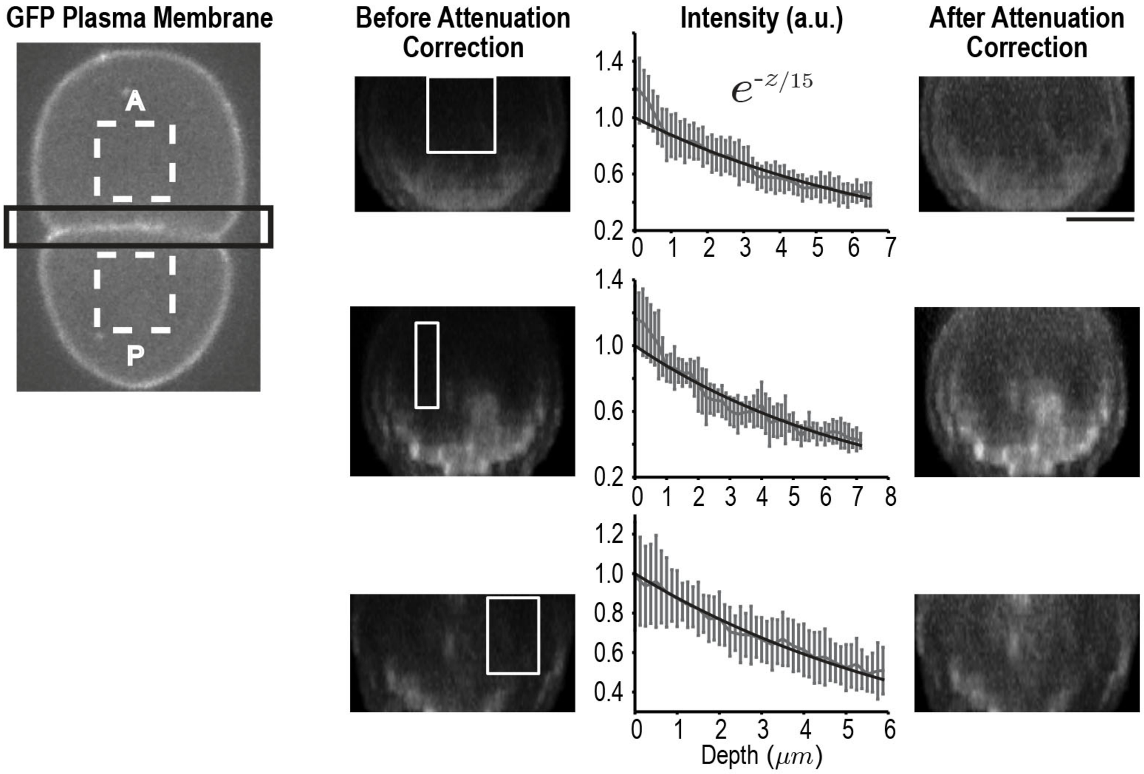

Figure 3 – Figure Supplement 4. Correcting for signal attenuation with sample depth. Fluorescence attenuation with embryo depth was estimated from fluorescence intensity measurements made at the cell-cell boundary of the 2-cell embryos expressing a GFP-tagged plasma membrane marker. Cell-cell boundaries were reconstructed from 40 plane z-stacks. The intensity profile at each slice was calculated by subtracting the average background intensity estimated from dashed rectangles (left) from the cell-cell boundary region (black rectangle) at each slice and calculating the maximum intensity projection along AP axis. The effect of depth on signal was calculated from the reconstructed division planes by plotting the mean signal as a function of depth in 10 rectangular regions (white boxes) where the signal was expected to be uniform; three examples are shown here. All intensity profiles were simultaneously fitted using a single exponential. Error bars are the SD. On the right, the same cell-cell boundaries are shown after correction for depth attenuation. The scale bar is 10 µm.

Figure 4

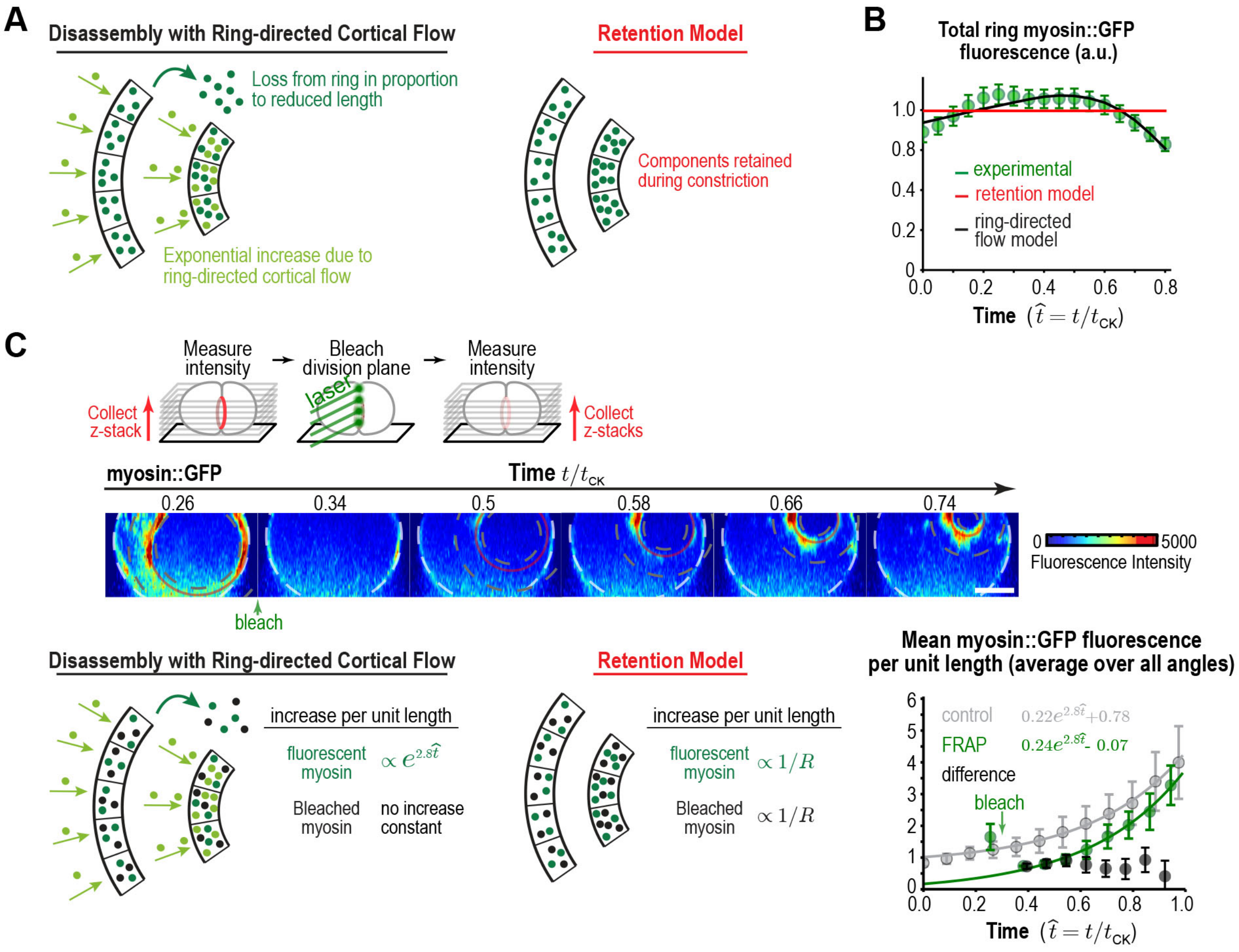

Figure 4. Recovery of myosin::GFP fluorescence after division plane bleaching supports delivery of myosin into the ring by ring-directed cortical flow. (**A**) (*left*) Two models that could explain the increase in the per unit length amount of myosin during constriction. (**B**) Graph plotting mean total ring fluorescence (average over all angles; *green*) for myosin::GFP with the predictions for the ring-directed cortical flow (*black*) and the retention (*red*) models (n= 36 embryos). Error bars are the SEM. (**C**) (*top*) Schematic of the photobleaching experiment to discriminate between the two models. (*middle*) Images of the division plane reconstructed from 30x1μm z-stacks of an embryo expressing myosin::GFP whose division plane was bleached at t/t_{CK} ~0.3. Red circle marks the contractile ring and dashed circles mark the boundaries used for ring intensity measurements. (*bottom left*) Schematics illustrate the expected concentration changes for fluorescent and bleached myosin::GFP. (*bottom right*) Graph plotting the mean per unit length amounts of fluorescent myosin::GFP in the ring for controls (*grey*, n=24 embryos) and after bleaching (*green*, n=8 embryos). The amount of bleached myosin::GFP in the ring (*black*), calculated as the difference between the control and FRAP curves is also shown. Continuous lines are exponential fits to the data. Error bars for controls and FRAP are SD and error bars for the difference are SEM. Scale bar is 10 μm. Image series in (**C**) is representative of 8 imaged embryos.

Figure 4—figure supplement 1

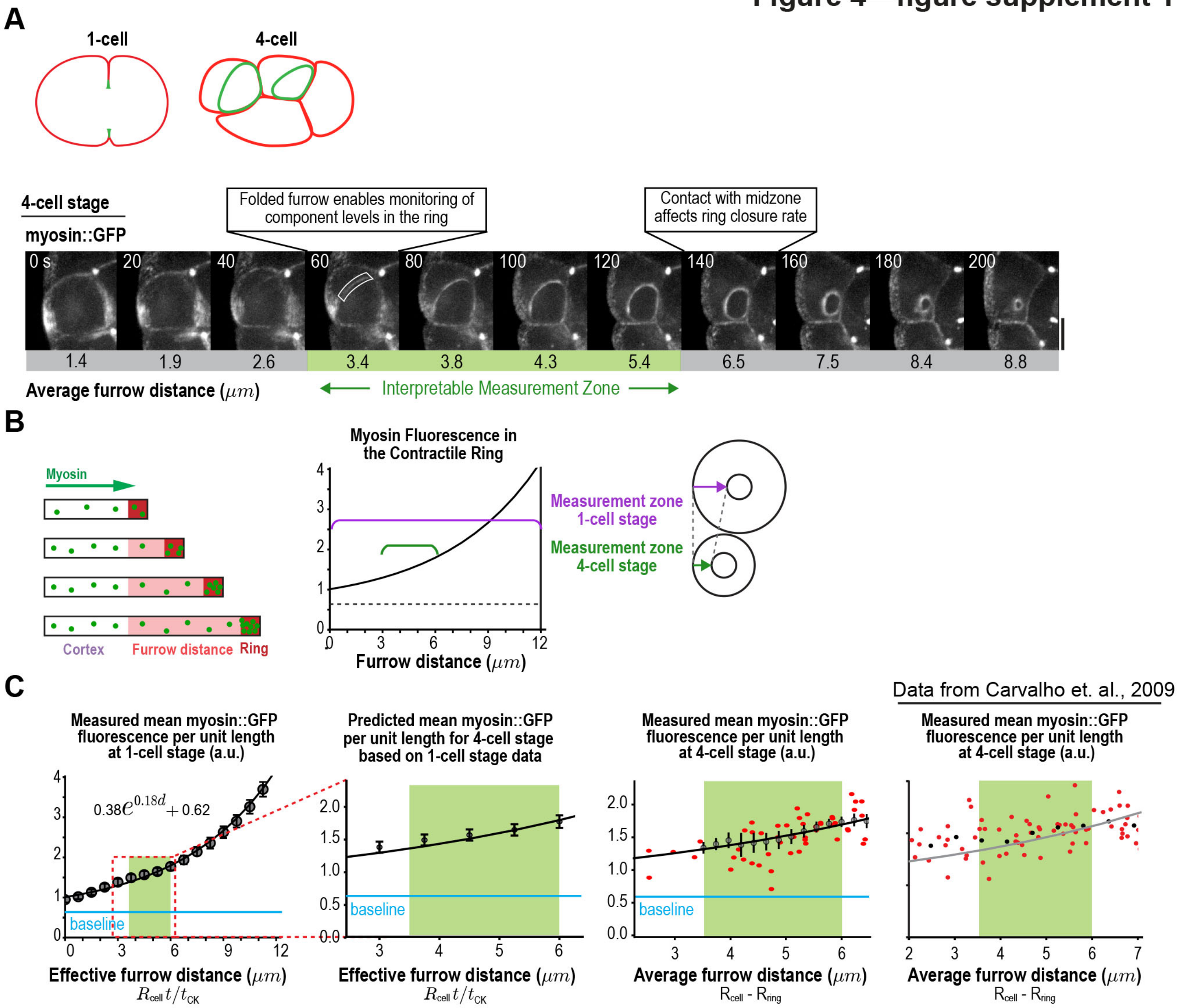

Figure 4 – Figure Supplement 1. Ring component levels in 4-cell stage embryos are consistent with accumulation due to ring-directed cortical flow. (**A**) At the 4-cell stage, cells often divide perpendicular to the imaging plane, providing an "end-on" view of the constricting ring relative to the imaging plane. However, a disadvantage of this division is that ~2/3 of the ring runs along sides of the cell in contact with neighboring cells and cannot be used for measurements. To be able to monitor component dynamics in the entire ring over a larger range of ingression distances, we therefore developed the quantitative tools described in this manuscript to monitor ring constriction at the 1-cell stage. *(top)* Schematic illustrating the relative geometries of cytokinesis in 1- and 4-cell stage *C. elegans* embryos. *(bottom)* images of the division plane in a representative dividing cell at the 4-cell stage reconstructed from 16x1μm z-stacks of an embryo expressing myosin::GFP (n=16 embryos imaged). (**B**) Our 1-cell stage analysis indicates that myosin levels in the ring increase exponentially as a function of furrow distance. The schematics show myosin::GFP fluorescence in the ring as a function of furrow

ingression distance at the 1-cell stage, and the predicted change as the furrow ingresses through the interpretable measurement zone at the 4-cell stage if ring myosin accumulates via the same mechanism. Detecting an exponential increase at the 4-cell stage is significantly more difficult than at the 1-cell stage because the cells are smaller and the distance that the furrow ingresses between its formation and when it contacts the spindle midzone, which slows furrowing (Carvalho et al., 2009), is about one quarter of what it is at the 1-cell stage (*Measurement zones*). (**C**) In comparing the 1- and 4-cell stage data, we took advantage of the fact that the initial per unit length constriction rates are the same at the two stages (Carvalho et al., 2009). This makes it possible to predict the pattern of myosin accumulation that we would expect at the 4-cell stage if ring myosin accumulates via the same mechanism that it does at the 1-cell stage, and compare it with measured values from the 4-cell stage. (*left panel*) One complication is that, while our 1-cell stage data show that myosin levels increase exponentially as a function of furrow distance, they also suggest there is a baseline of fluorescence (*cyan*) whose precise nature we do not understand—we postulate this baseline could correspond to myosin associated with the plasma membrane but not the cortex. This baseline signal is not part of the exponentially increasing population but influences the measured fold increase in total ring fluorescence. Curve fitting of the 1-cell stage data indicates that the exponentially increasing population increases ~9 fold as the furrow ingresses 12 μm; however, because of the baseline, the measured increase relative to initial ring fluorescence is only ~5-fold. (*middle and right panels*) At the 4-cell stage we can only measure ring component levels for furrow ingression distances between ~3 and 6 μm. The 1-cell data predicts that the exponentially increasing population, which is approximately equal to the baseline at 3 μm, would increase 1.7 fold by 6 μm, resulting in a 1.37-fold increase in total per unit length fluorescence. Fitting both new 4-cell data acquired with the *in situ* tagged myosin::GFP strain that we employed for the 1-cell analysis (*third panel*; n=14 embryos) and re-plotting our old data acquired using a myosin::GFP transgene (obtained from (Carvalho et al., 2009); *right panel*) revealed excellent agreement with the predicted curve (*grey line*). Error bars are the SEM. We conclude that data from 4-cell stage embryos are consistent with an exponential increase in ring components during ingression due to ring-directed cortical flow, but technical challenges make clear evidence for an exponential increase significantly more challenging to obtain during this stage relative to 1-cell stage embryos.

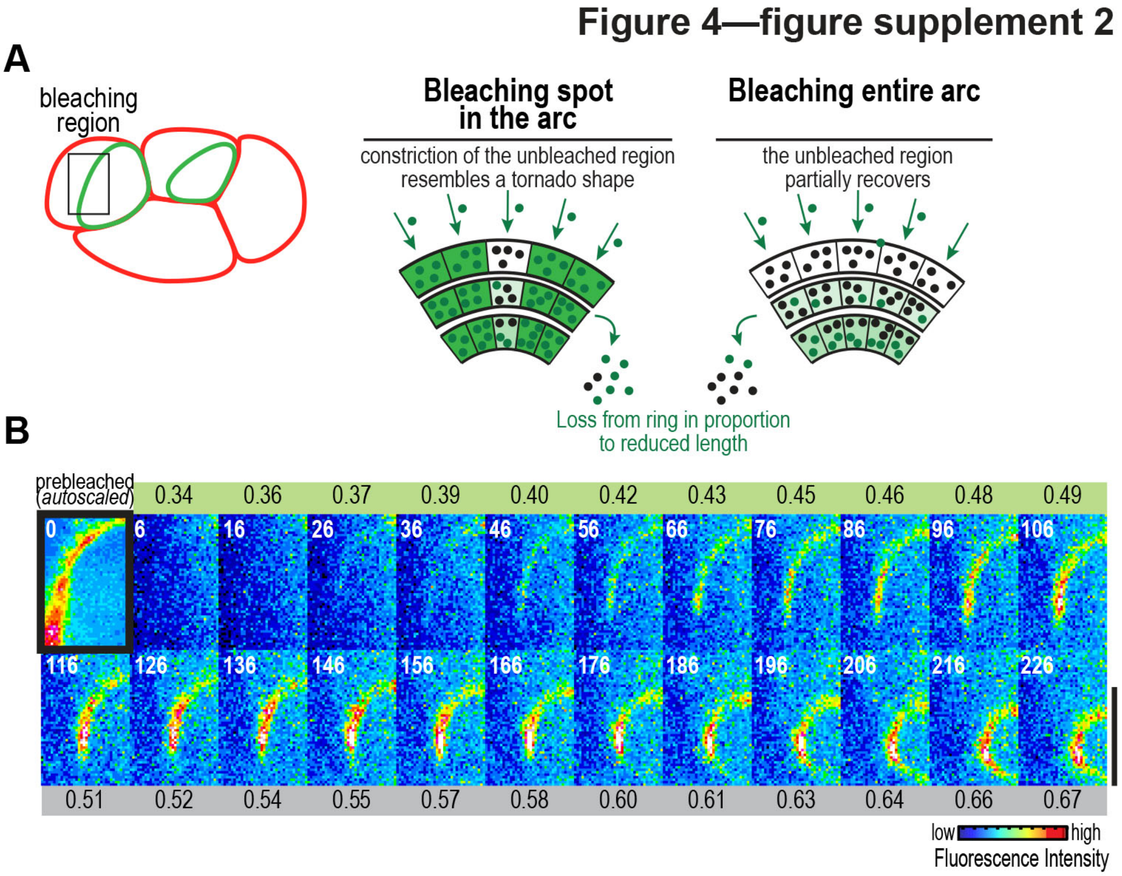

Figure 4 – Figure Supplement 2. Recovery of myosin::GFP fluorescence after division plane bleaching at the 4-cell stage supports delivery of myosin into the ring by ring-directed cortical flow. (**A**) We previously reported that following bleaching of a spot in the arc at the 4-cell stage, the bleached region progressively shrinks, generating a tornado shape in kymographs of a region drawn along the arc, and that the tornado thinning rate was slightly faster than predicted by shrinkage due to ring disassembly alone, which we could not explain (Carvalho et al., 2009). The disassembly with ring-directed cortical flow model that we propose here predicts that after photobleaching a spot in the arc, the unbleached fluorescence in the flanking regions will dominate the fluorescence of the bleached region and ring disassembly will cause the bleached region to progressively shrink, leading to a tornado shape in the kymograph. At the same time, cortical myosin, which turns over faster than myosin in the ring, will recover and ring-directed cortical flow will begin to deliver myosin to the ring again. The increase in ring fluorescence due to cortical delivery would accelerate the rate of tornado thinning consistent with our prior observations. (**B**) As a better test of whether ring-directed cortical flow delivers components to the ring at the 4-cell stage, we monitored recovery after photobleaching the entire contractile arc similar to the experiment that we performed at the 1-cell stage (**Figure 4C**). Images show a representative bleached embryo (n=10). The observed recovery pattern was very similar to what we observed at the 1-cell stage, supporting delivery by ring-directed cortical flow. Scale bar is 10 µm.

Figure 5

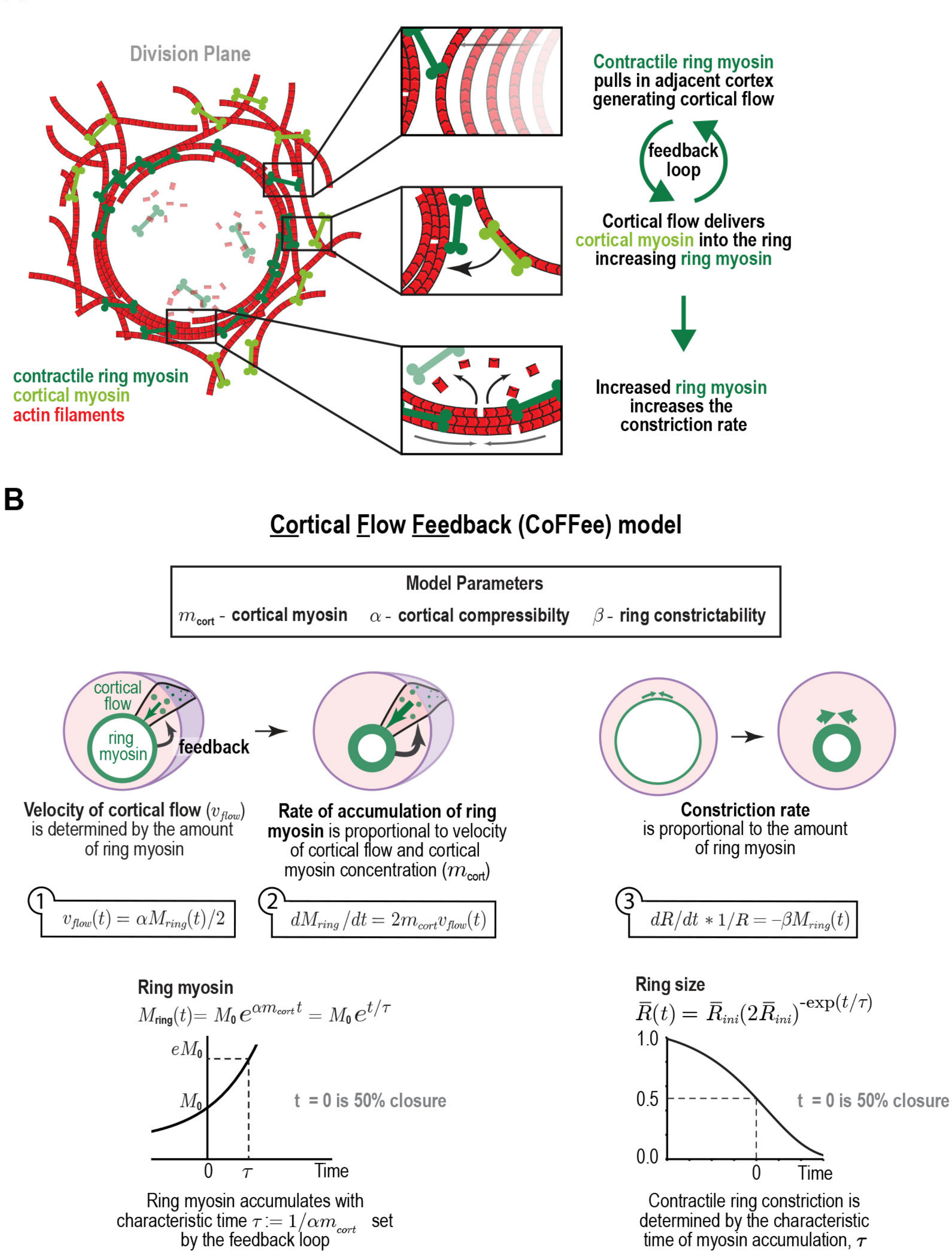
A
Division Plane
Contractile ring myosin pulls in adjacent cortex generating cortical flow
feedback loop
Cortical flow delivers cortical myosin into the ring increasing ring myosin
Increased ring myosin increases the constriction rate
contractile ring myosin
cortical myosin
actin filaments
B
Cortical Flow Feedback (CoFFee) model
Model Parameters
m_{cort} - cortical myosin
α - cortical compressibilty
β - ring constrictability
cortical flow
ring myosin
feedback
Velocity of cortical flow (v_{flow}) is determined by the amount of ring myosin
Rate of accumulation of ring myosin is proportional to velocity of cortical flow and cortical myosin concentration (m_{cort})
Constriction rate is proportional to the amount of ring myosin
1
$v_{flow}(t) = \alpha M_{ring}(t)/2$
2
$dM_{ring}/dt = 2m_{cort}v_{flow}(t)$
3
$dR/dt * 1/R = -\beta M_{ring}(t)$
Ring myosin
$M_{ring}(t) = M_0 e^{\alpha m_{cort} t} = M_0 e^{t/\tau}$
eM_0
M_0
0
τ
Time
t = 0 is 50% closure
Ring myosin accumulates with characteristic time $\tau := 1/\alpha m_{cort}$ set by the feedback loop
Ring size
$\bar{R}(t) = \bar{R}_{ini}(2\bar{R}_{ini})^{-\exp(t/\tau)}$
1.0
0.5
0.0
0
Time
t = 0 is 50% closure
Contractile ring constriction is determined by the characteristic time of myosin accumulation, τ

Figure 5. Cortical Flow Feedback (CoFFee) model of cytokinesis. (**A**) Schematic model incorporating the conclusions arising from our experimental analysis and proposed underlying molecular mechanism. (**B**) Formulation of the proposed mechanisms as an analytical mathematical model consisting of three equations and three model parameters that reflect properties of the cortex and ring. (*left*) Equations (1) and (2) describe the feedback loop between the amount of ring myosin and the velocity of cortical flow that leads to the exponential increases in the amount of ring myosin and the velocity of cortical flow. (*right*) Equation (3) describes the coupling of ring constriction to the amount of ring myosin.

Figure 6

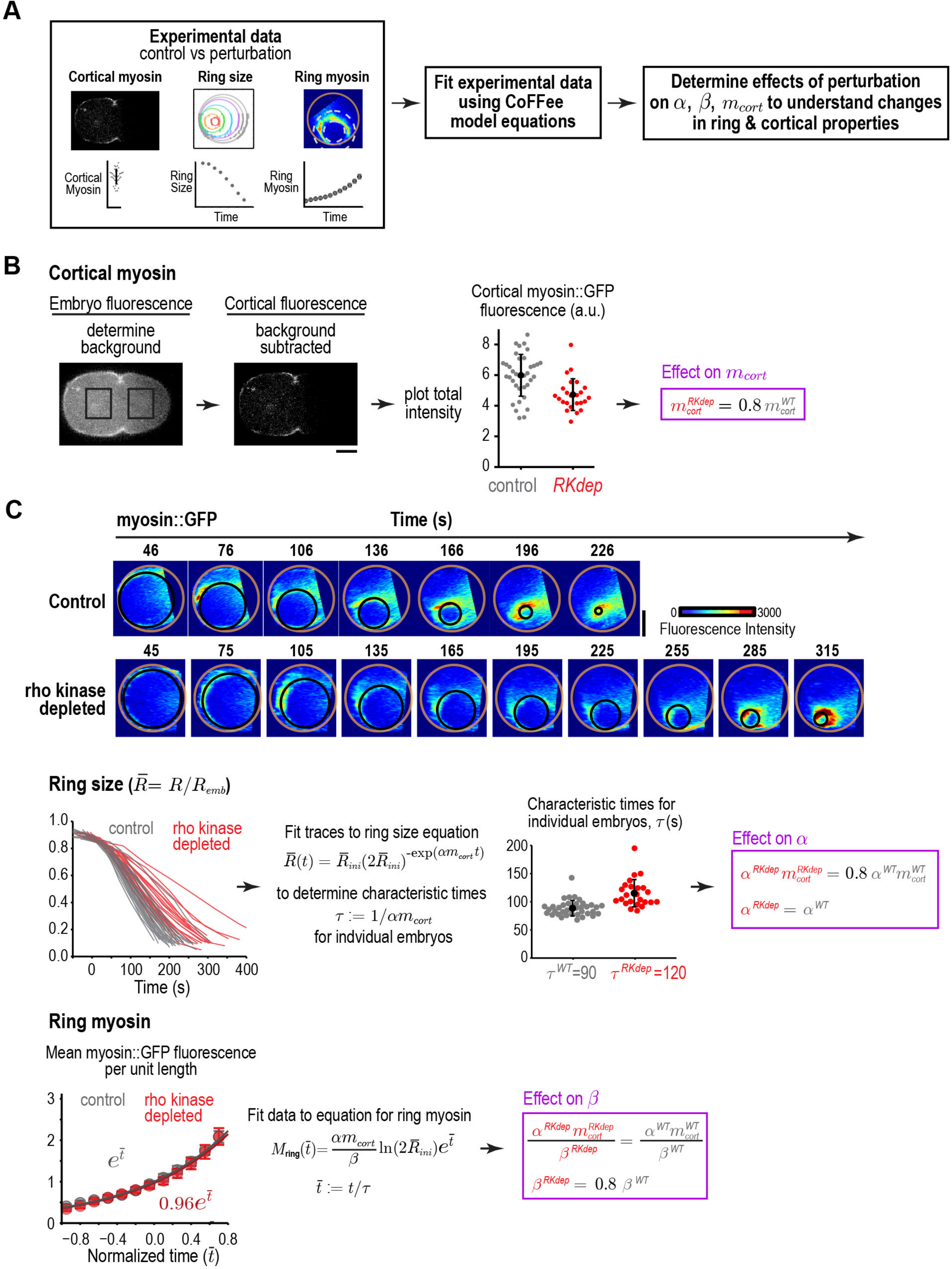
A
Experimental data
control vs perturbation
Cortical myosin
Ring size
Ring myosin
Cortical Myosin
Ring Size
Time
Ring Myosin
Time
Fit experimental data using CoFFee model equations
Determine effects of perturbation on α, β, m_{cort} to understand changes in ring & cortical properties
B
Cortical myosin
Embryo fluorescence
determine background
Cortical fluorescence
background subtracted
plot total intensity
Cortical myosin::GFP fluorescence (a.u.)
8
6
4
2
0
control
RKdep
Effect on m_{cort}
$m_{cort}^{RKdep} = 0.8\, m_{cort}^{WT}$
C
myosin::GFP
Time (s)
46 76 106 136 166 196 226
Control
0
3000
Fluorescence Intensity
45 75 105 135 165 195 225 255 285 315
rho kinase depleted
Ring size ($\bar{R}= R/R_{emb}$)
1.0
0.8
0.6
0.4
0.2
0.0
0 100 200 300 400
Time (s)
control
rho kinase depleted
Fit traces to ring size equation
$\bar{R}(t) = \bar{R}_{ini}(2\bar{R}_{ini})^{-\exp(\alpha m_{cort} t)}$
to determine characteristic times
$\tau := 1/\alpha m_{cort}$
for indvidual embryos
Characteristic times for individual embryos, τ(s)
200
150
100
50
0
τ^{WT}=90
τ^{RKdep}=120
Effect on α
$\alpha^{RKdep} m_{cort}^{RKdep} = 0.8\, \alpha^{WT} m_{cort}^{WT}$
$\alpha^{RKdep} = \alpha^{WT}$
Ring myosin
Mean myosin::GFP fluorescence per unit length
3
2
1
0
−0.8 −0.4 0.0 0.4 0.8
Normalized time ($\bar{t}$)
control
rho kinase depleted
$e^{\bar{t}}$
$0.96e^{\bar{t}}$
Fit data to equation for ring myosin
$M_{ring}(\bar{t}) = \frac{\alpha m_{cort}}{\beta} \ln(2\bar{R}_{ini}) e^{\bar{t}}$
$\bar{t} := t/\tau$
Effect on β
$\frac{\alpha^{RKdep} m_{cort}^{RKdep}}{\beta^{RKdep}} = \frac{\alpha^{WT} m_{cort}^{WT}}{\beta^{WT}}$
$\beta^{RKdep} = 0.8\, \beta^{WT}$

Figure 6. Fitting experimental data using the CoFFee model equations reveals the effects of rho kinase inhibition on cortical and contractile ring properties. (**A**) Flow chart illustrating how the CoFFee model can be used to fit experimental data to determine the effects of molecular perturbations on ring and cortical properties. (**B**) (*left*) images illustrating the method used to directly measure cortical myosin::GFP fluorescence. (*right*) Graph plotting cortical myosin::GFP fluorescence for control (*grey*, n=36) and rho kinase depleted (*red*, n=24) embryos. The mean and SD for each condition are shown in black. (**C**) (*top*) Images of the division plane in control and rho kinase depleted embryos expressing myosin::GFP. Gold circles mark the embryo boundaries and black circles mark the contractile ring. Image series shown are representative of the imaged embryos. Scale bar is 10 μm. (*middle, left*) Graphs of ring size traces for individual control (*grey,* n=36) and rho kinase depleted (*red*; n=24) embryos. (*middle, center*). Characteristic times, τ, for individual control (*grey*) and rho kinase depleted (*red*) embryos are plotted along with the mean and SD for each condition (*black*). (*bottom*) Graph plots mean myosin::GFP fluorescence per unit length (averaged over all angles with baseline subtraction) for control (*grey*) and rho kinase depleted (*red*) embryos. Error bars are SEM.

Figure 6—figure supplement 1

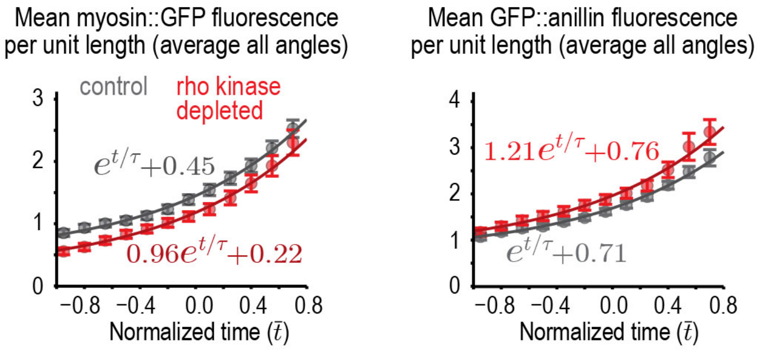

Figure 6 – Figure Supplement 1. Plots of mean myosin::GFP and GFP::anillin fluorescence in the ring versus time. Graphs plotting mean fluorescence per unit length (averaged over all angles) for GFP::anillin and myosin::GFP without baseline subtraction. Error bars are the SEM.

Figure 7

A

Effects of rho kinase depletion (from myosin::GFP data)

mechanical property	model parameter	value relative to wild type
cortical compressibilty	α	WT
cortical myosin	m_{cort}	0.8 WT
ring constrictability	β	0.8 WT

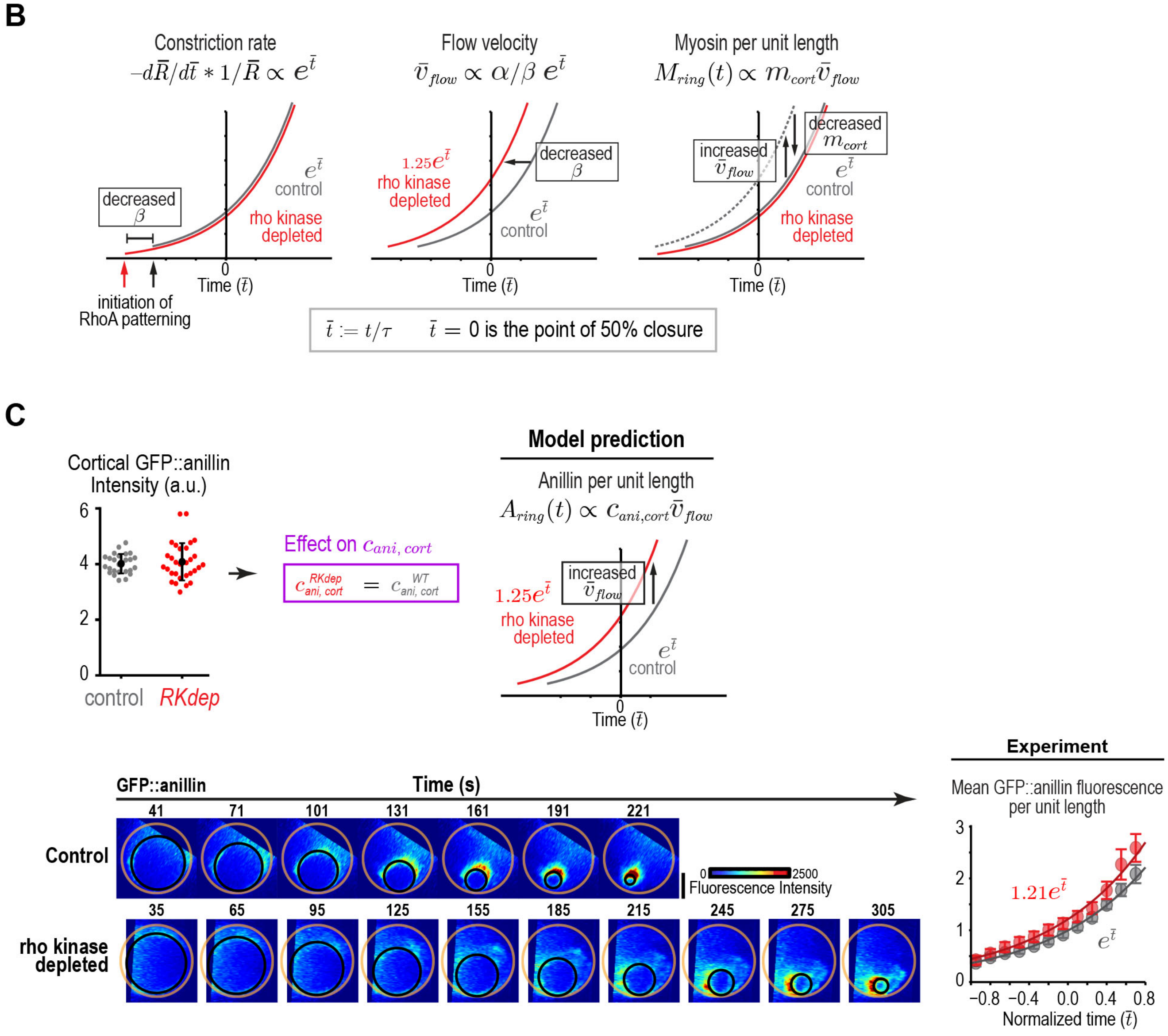

Figure 7. Reducing myosin activation by inhibition of rho kinase reduces the ability of the ring to be constricted by ring myosin. (**A**) (*top*) Table summarizing the effects of rho kinase depletion on model parameters. (**B**) Schematics summarizing the effects of rho kinase inhibition in the reference frame where time is normalized by dividing by τ and $\bar{t} = 0$ is 50% closure. In this time reference, comparing component levels and flow velocity at the same $\bar{t}$ corresponds to comparing them for the same ring size. (**C**) (*top, left*) Graph plotting cortical GFP::anillin fluorescence in control (n=25) and rho kinase depleted (n=30) embryos. The mean and SD are shown in black. (*top, right*) Since the concentration of cortical anillin is not changed, the increased cortical flow in rho kinase depleted embryos is expected to lead to a 1.25-fold increase in the per unit length amount of anillin for rings of all sizes. (*bottom, left*) Images of the division plane in representative control and rho kinase depleted embryos expressing GFP::anillin. Gold circles mark the embryo boundaries and black circles mark the contractile ring. (*bottom, right*) Data for mean GFP::anillin fluorescence per unit length (averaged over all angles with baseline subtraction) for control (*grey*) and rho kinase depleted (*red*) embryos reveals that ring anillin levels are increased 1.21-fold. Error bars are the SEM

Figure 7—figure supplement 1

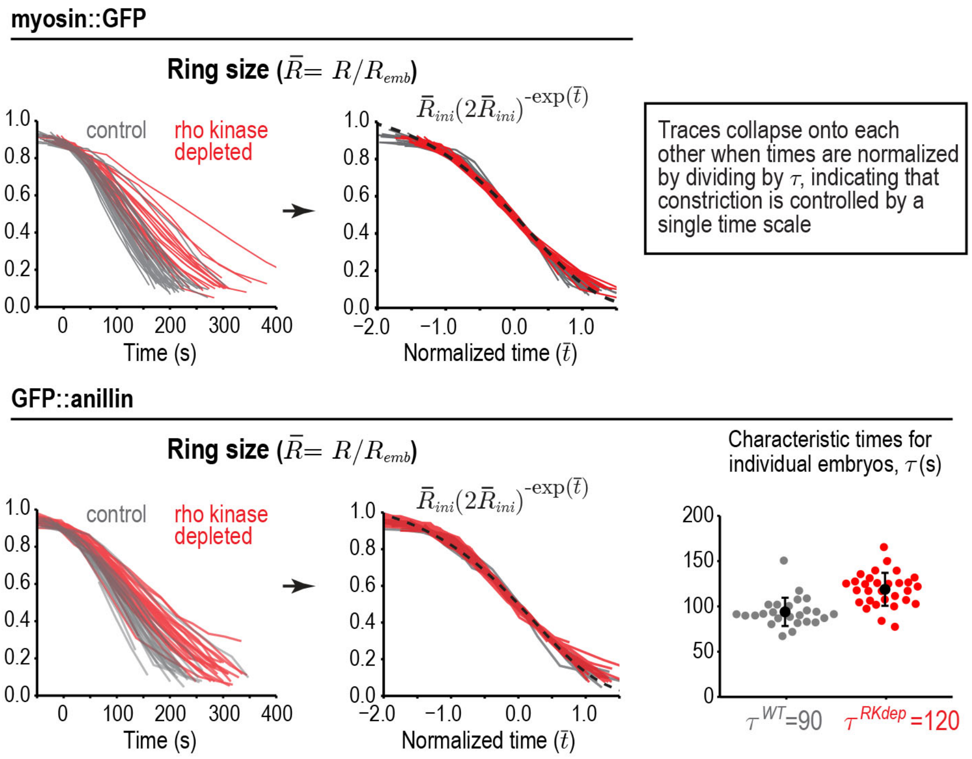

Figure 7 – Figure Supplement 1. Ring constriction is determined by a single time scale. Graphs of ring size traces for individual control (*grey,* n=36 myosin::GFP or 26 GFP::anillin) and rho kinase depleted (*red*; n=24 myosin::GFP or 30 GFP::anillin) embryos. Graph for myosin::GFP expressing embryos is reproduced from Figure 6C for comparison. Traces of ring size for all embryos collapse to the analytical curve (black dashed) when time is normalized by τ and $\bar{t} = 0$ is the point of 50% closure as expected if constriction is controlled by a single time scale. (*bottom, right*) Traces from GFP::anillin

expressing embryos were fit to the ring size equation to determine characteristic times, τ, for individual control (*grey*) and rho kinase depleted (*red*) embryos which are plotted along with the mean and SD for each condition (*black*). Rho kinase depletion increases τ 1.3-fold in GFP::anillin expressing embryos like it does in myosin::GFP expressing embryos.

Figure 7—figure supplement 2

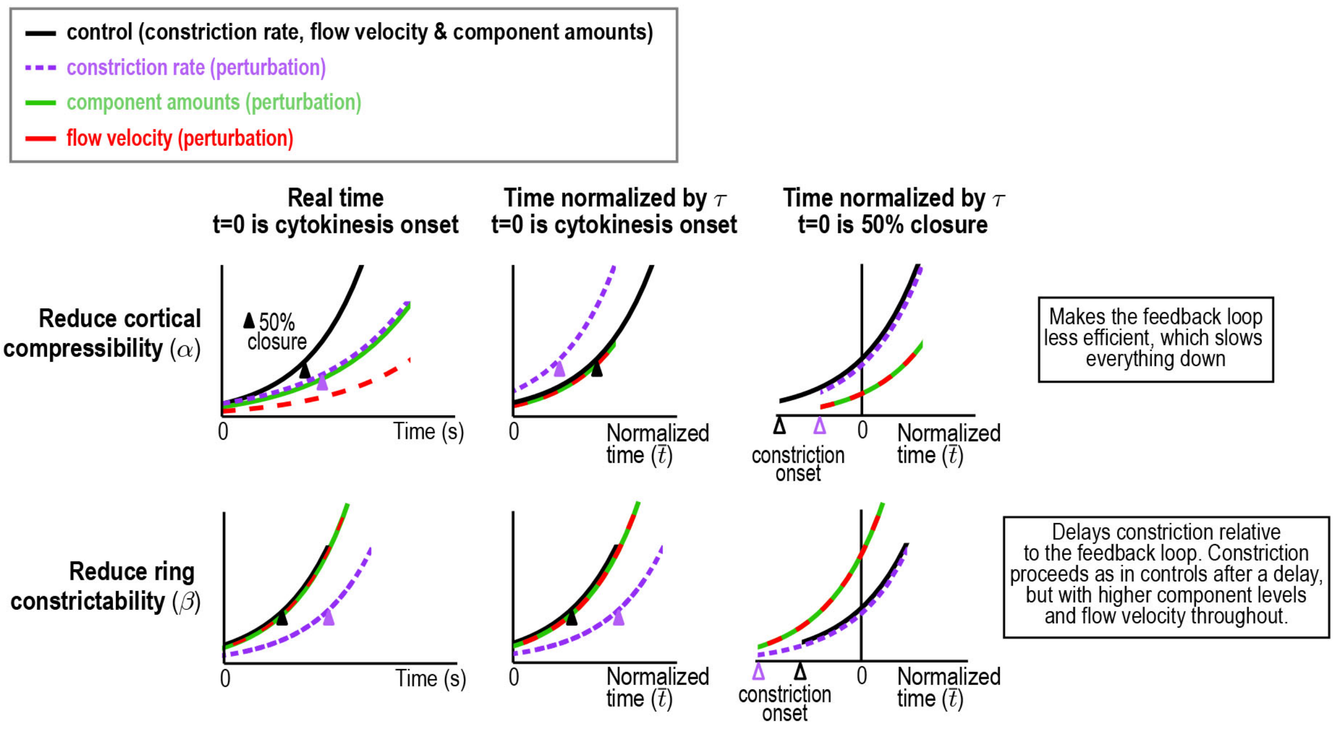

Makes the feedback loop less efficient, which slows everything down

Delays constriction relative to the feedback loop. Constriction proceeds as in controls after a delay, but with higher component levels and flow velocity throughout.

Figure 7 – Figure Supplement 2. Predicted effects of altering properties of the cortex or ring. Schematics illustrate the effects predicted by the CoFFee model of reducing the ability of ring myosin to compress the cortex (*top*) or constrict the ring (*bottom*) on the dynamics of per unit length component amounts (*green*), constriction rate (*purple dashed*) and cortical flow velocity (*red dashed*). The effect on each curve relative to control (*black*) is shown in three time references: real time with t=0 set to constriction onset (*left*), time normalized by τ with t=0 set to constriction onset (*center*), and time normalized by τ with t=0 set to 50% closure (*right*). (*top*) Perturbations that decrease cortical compressibility (α) would increase τ. (*top, right*) In real time, constriction rate and ring component amounts would increase with slower exponential kinetics ($\propto e^{t/\tau}$) from the same starting point as in controls, whereas flow velocity would increase with slower kinetics from a lower starting point ($\propto \alpha e^{t/\tau}$). (*top, center*) Normalizing time by τ, causes rates to be per τ; this increases the flow velocity and constriction rate curves by a factor of $1/\alpha$, bringing the flow velocity back to the control and making the constriction rate start at a higher value than in controls. (*top, right*) Setting t=0 to the 50% closure point superimposes the constriction rate curve with the control, causing the curves for ring component

amounts and flow velocity to fall below the controls. Since comparing properties for the same $\bar{t}$ in this reference is equivalent to comparing properties for a given ring size, reducing α would lead to a reduction in component amounts for all ring sizes. (*bottom*) Reducing ring constrictability (β) does not affect τ. (*bottom, left*) In real time, flow velocity and ring component amounts increase with the same exponential kinetics as controls from the same staring point. The constriction rate also increases with the same exponential kinetics as in controls, but from a lower starting point due to the reduced β. Due to the exponential nature of the curves, the lower starting point effectively introduces a temporal offset, delaying constriction relative to the curves for ring component amounts and flow velocity. (*bottom, center*) Since reducing β does not affect τ, normalizing time by τ does not affect the relationship between the curves. (*bottom, right*) Setting t=0 to the 50% closure point superimposes the constriction rate curve with the control and reveals that reducing β would lead to an increase in component amounts and flow velocity for all ring sizes.

SUPPLEMENTARY VIDEO LEGENDS

Video 1. Cortical flow imaged in a control embryo expressing myosin::GFP. Playback is 6x realtime. The video is constructed from maximum intensity projection of 3 x 0.75 µm plane z-stacks acquired at 2 s intervals. The red line marks the position of the division plane. The arrows represent the surface movement between consecutive frames at the base of the arrow. The length of the arrow is 5 times the magnitude of movement. The direction is also color coded according to the color wheel as shown in Figure 1b.

Video 2. Average cortical flow map calculated from time lapse imaging of the cell surface in 93 control embryos expressing myosin::GFP. (*top, left*) Schematic illustrates location of the cylindrical surface covered by the map. (*top, right*) Dynamic schematic illustrates ring size and position for each value of t/t_{CK}. (*bottom, left*) The movement of each blue dot corresponds to surface movement at its location. The y-axis is the angular position relative to the initial ingression axis. The x-axis is the distance from the division plane along the anterior-posterior axis. (*bottom, right*) Dynamic graph plots the magnitude of the component of surface velocity aligned along the anterior-posterior axis for the top (150-180°; black) and bottom (0-30°; grey) regions of the cortex.

Video 3. Average cortical flow map calculated from time lapse imaging of the cell surface in 68 *arx-2(RNAi)* embryos expressing Myosin::GFP. (*top, left*) Schematic illustrates the location of the cylindrical surface covered by the map. (*top, right*) Dynamic schematic illustrates ring size and position for each value of t/t_{ck}. (*bottom, left*) The movement of each blue dot corresponds to surface movement at its location. The y-axis is the angular position relative to the initial ingression axis. The x-axis is the distance from the division plane along the anterior-posterior axis. (*bottom, right*) Dynamic graph plots the magnitude of the component of surface velocity aligned along the anterior-posterior axis for the top (150-180°; black) and bottom (0-30°; grey) regions of the cortex.